This manuscript is a preprint and has been submitted to Tektonika. This manuscript has not undergone peer-review. Subsequent versions of the manuscript may have different content. If accepted, the final version of this manuscript will be available via the "Peer-reviewed Publication" DOI link on this webpage. Please feel free to contact the authors directly to comment on the manuscript. We welcome feedback!

The cyclical nature of normal fault growth: Insights from 4D analogue models

B. Lathrop [1, 2*], F. Zwaan[3, 4, 5], T. C. Schmid[4], C. A.-L. Jackson [1], R. E. Bell[1], A. Rotevatn[6], G. Schreurs[4]

[1]Department of Earth Science and Engineering, Landscape and Basins Research Group (LBRG), Imperial College London, London, UK

[2]School of Geographical and Earth Science, University of Glasgow, Glasgow, UK

[3]Helmholtz Centre Potsdam - GFZ German Research Centre for Geosciences, Potsdam, Germany

[4]Institute of Geological Sciences, University of Bern, Bern, Switzerland

[5]Department of Geosciences, University of Fribourg, Fribourg, Switzerland

[6]Department of Earth Science, University of Bergen, Bergen, Norway

**Corresponding author (e-mail: Bailey.lathrop@glasgow.ac.uk)*

Abstract

Exploring how normal faults evolve is important for understanding the dynamic processes underlying the initiation and evolution of rift systems. Early-stage fault growth has been largely under-explored due to resolution limitations in seismic reflection data and the lack of three-dimensional exposures in the field. Physical analogue modelling offers a unique way to visualize and analyse early-stage fault growth. Here, we present results from an innovative analogue modelling approach that allows us to resolve fault growth in 4D through the use of a medical-grade, X-ray computed tomography (CT) scanner, as well as top-view time-lapse photography and digital image correlation (DIC) analysis.

We show that faults establish their vertical height at the earliest stage of deformation and laterally grow via a cyclical growth pattern, alternating between periods of rapid lengthening associated with relay-breaching and segment linkage, and periods characterised by throw accumulation. As extension continues, strain is partitioned onto increasingly fewer, optimally spaced and orientated faults, which continue to lengthen via segment linkage; faults in stress shadows, and/or with double conjugate boundaries, become inactive. It is the first time that fault lengthening and throw have been tracked in 4D with such high-fidelity and that this style of cyclical fault growth has been resolved, representing significant advances in our understanding of normal fault growth from segment-scale to network-scale, made possible only by the innovative use of X-ray CT-scanning.

1. Introduction

Understanding how normal faults grow provides important insights into the distribution of extensional strain (e.g., Gupta et al., 1998; Cowie et al., 2000; Meyer et al., 2002; Walsh et al., 2003) and the tectonostratigraphic development of rift basins (e.g., Gawthorpe & Leeder, 2000; McLeod et al., 2002; Ge et al., 2017; Henstra et al., 2017; Jackson et al., 2017; Rotevatn et al., 2019; Pan et al., 2021, 2022; Carpenter et al., 2022). The growth of normal faults has historically been described by two end-member models: (1) the propagating fault model and (2) the constant-length model (Figure 1). According to the propagating fault model, faults grow via a synchronous increase in fault length and displacement/throw (e.g., Walsh & Watterson, 1988; Dawers et al., 1993; Cartwright et al., 1995; Walsh et al, 2003). By contrast, the constant-length model states that faults reach their near-maximum length relatively quickly, after which they grow mainly by accrual of displacement/throw (e.g., Walsh et al., 2002, 2003; Nicol et al., 2005, 2020; Jackson & Rotevatn, 2013; Tvedt et al., 2016; Rotevatn et al., 2019; Sahoo et al., 2020; Carpenter et al., 2022). Several studies (e.g., Jackson et al., 2017; Rotevatn et al., 2019; Nicol et al., 2020b) suggest that faults likely follow a hybrid model of the two, adhering to the propagating fault model for the first 20-30% of their lifespan and the constant-length model for the remainder (Figure 1) (see also Finch and Gawthorpe, 2017). A step-wise or cyclical fault growth model has also been suggested (Cartwright et al., 1996; Filbrandt et al., 2007; Schlagenhauf et al., 2008; Pan et al., 2021), whereby faults grow via alternating phases of lengthening and displacement/throw accumulation, with faults in stress shadows becoming inactive as strain localises onto optimally placed faults (Figure 1). This hypothesis has not yet been verified, however, likely because: 1) syn-kinematic (growth) strata from the earliest stage of faulting, which can provide a direct record of early-stage fault growth (e.g., Childs et al., 2003; Jackson et al., 2017), are poorly imaged/resolved in seismic reflection data due to being thin and/or deeply buried; 2) the spatial resolution of typical industry airgun seismic reflection datasets means that only faults with >5-10 meters of displacement, and stratigraphic units of comparable thickness, will be imaged (Pickering et al., 1997; Faleide et al., 2021), and 3) growth strata are often poorly exposed in the field.

Analogue tectonic models, however, can offer unique insights into early-stage normal fault growth patterns and the development of rift basins, given they allow us to: (i) directly observe incremental changes in their geometry (e.g., displacement/throw and length) and kinematics (e.g., initiation, slip rate, and fault death); and (ii) assess the impact of various parameters on fault and rift development, including extension obliquity and pre-existing structures (e.g., Vendeville et al., 1987; Mansfield & Cartwright, 2001; Hus et al., 2005; Filbrandt et al., 2007; Schlagenhauf et al., 2008; Whipp et al., 2016; Zwaan et al., 2016, 2019; 2021a, b; Chauvin et al., 2018; Rotevatn et al., 2019; Osagiede et al. 2021; Wang et al., 2021; Carboni et al., 2022; Schmid et al., 2022a). However, the analysis of analogue models is traditionally based on overhead (i.e., top-view) images of the model top surface and side-view images taken through transparent sidewalls (e.g., Schlagenhauf et al., 2008; Mayolle et al. 2023, see Zwaan et al. 2022 and references therein). Due to the opaque nature of the modelling materials used in such models, fault geometries and evolution at depth, the temporal changes in the subsurface geometry of individual faults or the fault network as a whole, and/or how these might relate to their surficial expression (e.g., segmentation), cannot be directly assessed.

In this paper, however, we present the results of an innovative approach that allows us to track fault growth in three-dimensional space *and* through time (4D) in an analogue rifting model, made possible by the combined use of a medical-grade X-ray computed tomography (CT) scanner and overhead image analysis. We focus on how fault length, throw, and height change through time (including the early, previously un-resolved stages of fault growth), and how these changes in geometric parameters relate to fault segment interaction and linkage. This is the first time that changes in fault length and throw have been tracked at such close temporal intervals and in fully three dimensions.

2. Methodology

2.1. Model materials

Granular materials are routinely used to simulate brittle parts of the lithosphere. In this study, we use quartz sand from Carlo AG (ø = 60-250 μm) (www.carloag.ch; Zwaan et al. 2018) to represent the upper crust. The sand is sieved from ~30 cm above the model surface to guarantee a density of ~1560 kgm^{-3} (Schmid et al., 2020c), with the sand subsequently flattened with a scraper at every 1 cm to create stratigraphic layering (e.g., Zwaan et al., 2019). We then add a thin (c. 1 mm) dusting of denser (1890 kgm^{-3}) corundum sand every 1 cm to create a slight density contrast that would make layering visible on CT scans. The angles of internal peak and stable friction are 36.1° and 31.4°, respectively, for the quartz sand, and 37° and 32° for the corundum sand (Zwaan et al., 2018); both types of sand have very similar mechanical properties, thus adding layers of corundum sand as marker intervals does not significantly alter the model development or more specifically, the fault geometry and kinematics (e.g., Zwaan et al., 2016; Zwaan & Schreurs, 2017).

The bottom viscous layer, which simulates the ductile lower crust, is 4 cm-thick and consists of a near-Newtonian (viscosity η; ca. $1.5x10^5$ Pa s; stress exponent η=1.06-1.10; Zwaan et al., 2018) viscous mixture of SGM-36 polymethylsiloxane (PDMS) silicone (manufactured by Dow Corning) and the same corundum sand is used for layering in the overlying sand layer described above (ρ specific = 3950 kg m^{-3}; Panien et al., 2006; Zwaan et al., 2016, 2019). This silicone/corundum sand mixture is mixed at a 1:1 weight ratio to have a similar density to that of quartz sand (~1560 kgm^{-3}), preventing the viscous layer from buoyantly rising in an unrealistic manner (Zwaan et al., 2016, 2019). The properties of the model materials are summarised in Table 1.

2.2. Model set-up

The general model apparatus we use for our rifting model is the same as the one applied by Zwaan et al. (2016; 2019; 2020; 2021a, b) (Figure 2). This apparatus contains a fixed base plate with two sidewalls that move independently of each other, their motion controlled by precise, computer-guided motors.

The base of the model set-up consists of alternating 1 cm-wide strips of RG 50 polyurethane foam and 5 mm-wide plexiglass strips which is placed on top of the fixed base plate, above which the brittle and viscous model layers are added (Figure 2). Note that no seed (i.e., a structural weakness) is applied at the base of the brittle sand layer to initiate rifting, as has been done in previous models using this same apparatus (Zwaan et al., 2016, 2019, 2021a, b), and in other analogue models (Le Calvez et al., 2002; Filbrandt et al., 2007; Liang et al., 2021; Osagiede et al., 2021; Schmid et al., 2022a, b). Instead, the model is relatively free to develop faulting in the sand layer, thus permitting the “natural” initiation and evolution of the arising fault network.

The sidewalls are moved apart by a total of 4 cm (i.e., each sidewall 2 cm), and the model set-up base is compressed prior to addition of the brittle-viscous model materials; this allows the model to expand uniformly as the sidewalls move apart during the model run.

As a result, the overlying model materials are extended, and the model reaches a final width of 34 cm. The model is extended at a rate of 400 mm/hr, which is a relatively high extension rate compared to previous studies using this apparatus (rates between 3 mm/hr and 100 mm/hr; Zwaan et al., 2016; 2019; 2020; 2021a, b). We apply this relatively fast rate given this was needed to form any structures within the sand pack, without the use of a seed or other pre-defined weakness. Extension is briefly stopped every 2 mm of extension for the model to be CT-scanned, which is not considered to have significantly affected model evolution. Information on scaling can be found section 1 of the Appendix.

2.4. Model monitoring and analysis

Two Nikon D810 (36 MP) DSLR cameras mounted above the model apparatus and oriented at an angle of c. 30° take time-lapse photos of the model surface throughout extension, at fixed increments of 2 mm. Markers with known coordinates are placed in each corner of the apparatus for geo-referencing. To quantify surface deformation, we apply digital image correlation (DIC) analysis, which tracks particle patterns as they displace throughout the duration of the model run (e.g., Adam et al., 2005; Boutelier et al., 2019; Zwaan et al., 2020, 2021a, b, Schmid et al., 2022a, b). For the DIC analysis, the model area is subdivided into small interrogation windows for which local displacement vectors are calculated on subsequent images using a cross-correlation algorithm. The resulting local displacement vectors are assembled into incremental displacement maps for the in-plane displacement components u_x and u_y. Postprocessing includes outlier filtering to detect spurious vectors within a 3 x 3 neighbourhood (Westerweel and Scarano, 2005) and their replacement by an iterative interpolation requiring at least two adjacent vectors.

For quantifying onset, duration, and intensity of faulting, we use the small strain tensor e obtained from displacement gradients with:

$$e_{ij} = \frac{\partial u_i}{\partial x_j} \qquad (1)$$

with the components,

$$e = \begin{bmatrix} e_{xx} & e_{xy} \\ e_{yx} & e_{yy} \end{bmatrix} \qquad (2).$$

We show the quantitative deformation evolution in strain maps using the maximum principal strain e_{max}. In contrast to the components of the small strain tensor, e_{max} is independent of the coordinate system and is obtained from e via

$$e_{max} = \frac{e_{xx} + e_{yy}}{2} + \sqrt{\left(\frac{e_{xx} - e_{yy}}{2}\right)^2 + e_{xy}^2} \qquad (3).$$

For analysing the spacing evolution of active faults, we create extension-parallel swath profiles (20 mm width) of incremental e_{max}values at the model centre (i.e., x = 0 mm). For each time step, values are normalized using the maximum occurring value for comparison.

To reveal its internal evolution, the model is scanned using a medical X-ray CT scanner (64 slice Siemens Somatom Definition AS X-ray CT-scanner). The CT scan volumes consist of single image slices perpendicular to the long model axis (and parallel to the experimental extension direction) with a resolution of ~0.72 x 0.72 mm/pixel (given a scan matrix of 512 x 512 pixels and a 370 x 370 mm scan window) and a slice thickness of 0.6 mm. The scan images are converted from DICOM files (the standard format for CT files) into SEG-Y files (the standard format for seismic data) using the software GeoAnalog, so that images can be loaded into and interpreted within Petrel seismic interpretation software in a similar manner to a 3D seismic reflection volume (i.e., with inlines, crosslines and depth slices).

The terminology used to describe the geometry of the fault network is shown in Figure 3, with additional information on overlapping faults and fault segment interaction provided in Section 2 of the Appendix. Fault throw and length are measured at every time step (every 2 mm of extension), starting from 22 mm of extension, when the faults have sufficiently large throws to be imaged and thus measured in the 3D CT dataset. We use cardinal directions to describe the models, i.e., one side of the CT-scanned model is north, and the opposite side is south (see Figure 2).

3. Results

In this section we qualitatively describe the overall structural development of the model, from the initiation to the cessation of extension. We then focus on three segmented faults in order to quantify how they evolve, focusing on fault development between 22 mm of extension and 40 mm of extension, i.e., towards the end of extension.

3.1. Overview of fault expression and evolution

Faulting along the long axis of the model can first be seen after 6 mm of extension (Figures 4 and 5), although these are considered edge effects (see Zwaan et al., 2016, 2019). Due to the higher resolution of the top-view images compared to the CT scans, the overhead DIC analysis can image fault activity earlier than observed in the CT scans. For example, some incipient faulting across the centre of the model can be seen at around 8 mm extension in the overhead images (Figure 4) and at around 12 mm extension in the CT scan (Figure 5). From 10-14 mm extension, there are many closely spaced, seemingly low-throw faults observed both in the DIC results and CT scans (Figures 4 and 5). Between 20-22 mm extension (Figures 4 and 5), some faults appear to become more active, or at least are characterised by better-defined surface traces. Fault traces can be mapped at depth by 22 mm extension, and at that point, faults have already reached their maximum height, spanning the base of the model to the surface. In the later stages of the model run (post-26 mm extension), longer and better-developed faults start to form grabens. Small and low activity faults can be seen between the larger structures (Figures 4-5). Faults maintain a constant dip of ~64° throughout the model run (see section 4.1).

Even though throw is too low to be directly visible at the earliest stages of faulting in the more qualitative top view strain maps (Figure 4) and the CT scanner images at shallow depth (Figure 5), the swath profile analysis allows strain distribution to be quantified across the top of the model from the earliest stages of extension on, showing the number of active faults, fault spacing, as well as strain localisation throughout the extension of the model (Figure 6 and Supplementary Figures 10-13). Maxima in the e_{max} swath profiles across the centre of each model delineate active faults (Figure 6).

The spacing and amount of active faults changes between the early and later stages of the model (Figure 6). At 6 mm extension, there are ~25 active faults across the swath profile, faults are spaced an average of ~1.1 mm apart, and the percentage of normalised strain on each fault is between 4-8% (Figure 6a). At 14 mm and 22 mm extension, there are ~23 active and ~21 active faults across the swath, faults are spaced ~1.05 and ~0.95 mm apart, and normalised strain on faults is between ~0.2-0.9 and ~0.1-0.75, respectively (Figure 6b-c). At 30 mm extension, there are ~20 active faults spaced ~0.8

mm apart, with normalised strain on faults varying from ~0.5-0.9 (Figure 6d). At 38 mm extension, there are ~16 active faults, spaced ~0.6 mm apart, and normalised strain on faults varies from ~0.05-0.95; only four faults have a normalised strain >0.25 (Figure 6e). Generally, as extension continues, the number of active faults decrease, the spacing between faults increases, and the amount of strain on different faults across the width of the model becomes more varied, with more strain being accommodated onto increasingly fewer faults.

3.2. Detailed fault analysis

Having looked at the general patterns and styles of fault network development, we will now focus on three specific segmented faults, tracking temporal changes in their length and throw. We chose these three faults (F1-3) because they have sufficient throw to be imaged relatively early in the model run, and because they show different types of interactions with adjacent faults. These three faults are labelled in CT scan images in Figure 7.

3.2.1. Fault 1

On the model top surface, F1 is 650 mm long and has a maximum throw of 30 mm at the end of extension (Figure 8). The shape of its throw length profile at maximum extension is generally symmetrical and bell-shaped with two throw maxima (Figure 8D). It has a N-S strike and dips to the E (Figure 7). F1 consists of three segments (referred to as F1A-C) that are initially separate, but which eventually link via tip propagation and linkage (Figure 8). At its final length, F1 has a conjugate fault boundary (see Figure 3) at its northern tip and a synthetic boundary at its southern tip.

At 22 mm of extension, the segments comprising F1 are not linked and their tips are underlapping (Figure 8a). The length and throw of F1C at this time are 120 mm and 1 mm, respectively (Figure 8a). Subsequently, between 22 mm and 28 m of extension, the tips of F1A-C propagate, such that the tips of F1B and F1C overlap, although the segments themselves are not physically linked (Figure 8b). F1A eventually physically links with F1B at 32 mm of extension (Figure 8b), meaning the length and throw of the now-linked segments are 340 mm and 9 mm, respectively (Figure 8b). Before F1A and F1B physically link, their tips did not overlap, resulting in tip-to-tip linkage (Figure 8b). Between 32 and 36 mm of extension, F1AB lengthens to 380 mm and accrues a total of 19 mm of throw (Figure 8c). At 38 mm of extension, the relay between F1A-B and F1C is breached (Figure 8c), bringing the total length and throw of the newly formed fault to 640 mm and 24 mm, respectively (Figure 8c). The length of F1 then remains relatively stable (up to 650 mm), although the maximum throw increases to 30 mm by the end of extension (Figure 8d).

3.2.2. Fault 2

F2 is 900 mm long and has a throw of 31 mm at the end of extension (Figure 9). The shape of its throw length profile at maximum extension is generally asymmetrical and bell-shaped with two throw maxima (Figure 9C). It strikes N-S and dips to the E (Figure 7). F2 consists of two segments (referred to as F2A-B) that are initially separate, but which eventually link (Figure 9). F2 has a synthetic fault boundary at its northern tip and a free southern tip, noting that the southern tip is close to the edge of the model (Figure 9).

At 22 mm of extension, the tips of segments F2A and F2B are underlapping and F2 is surrounded by many small, low-throw faults (Figure 9a). At this time, F2A is 460 mm long and has a throw of 2 mm (Figure 9a). Subsequently, between 22 and 30 mm of extension, F2A grows by tip propagation, and has total length and throw of 550 mm and 13 mm, respectively (Figures 9b). The tips of F2A and F2B overlap at 30 mm extension and the relay ramp between the segments breaches at 32 mm extension (Figure 9b), and the now-linked F2 has a length and throw of 820 mm and 15 mm, respectively (Figure 9b). Between 32 mm and 40 mm of extension, F2 grows slightly via tip propagation, bringing its final length and throw to 900 mm and 31 mm, respectively (Figure 9c).

3.2.3. Fault 3

F3 is 1550 mm long with a maximum throw of 40 mm at the end of extension (Figure 10). It strikes N-S and dips to the W (Figure 7). The shape of its throw length profile at maximum extension is asymmetrical and triangular with two main throw maxima (Figure 10D). F3 consists of three segments (referred to as F3A-C) that are initially separate, but which eventually link (Figure 10). Both the northern and the southern tips of F3 have conjugate boundaries with adjacent segments (Figure 10).

At 22 mm of extension, F3B has a length of 680 mm and a throw of 2 mm, whereas F3A and F3C are not yet resolvable until 24 mm and 26 mm of extension, respectively (Figure 10a; Supplementary Figure 16). Between 22 mm and 26 mm extension, F3B lengthens slightly via tip propagation to 690 mm, and accumulates a throw of 6 mm (Figure 10b). At 28 mm extension, F3A and F3B overlap and the relay ramp between them breaches, bringing the total length and throw of the now-linked system to 1280 mm and 7 mm, respectively, while the tips of F3B and F3C overlap but remained unlinked (Figure 10b). Between 28 mm and 32 mm of extension, F3A/B accumulates a total of 20 mm of throw and lengthen to 1340 mm (Figure 10c). The relay ramp between F3A/B and F3C is breached at 34 mm of extension, bringing the total length and throw of the now-linked system (i.e., F3) to 1530 mm and 30 mm, respectively (Figure 10c). Between 34 and 40 mm of extension, F3 does not appreciably lengthen (1530 mm total), whereas throw increases to 40 mm by the end of extension (Figure 10d).

4. Discussion

The throw and length of three faults (and their associated segments) are measured at every 2 mm of extension, from 22 mm to 40 mm (Figures 8-11). These faults show a cyclical pattern of growth, comprising periods of rapid lengthening followed by prolonged throw accumulation. Here we will compare the results of our model to previous analogue modelling studies and to data from natural examples of normal faults, exploring the validity of cyclical fault growth model, as well as discussing the processes and products of strain localisation within fault networks.

4.1. Comparison to natural faults and previous physical analogue model studies

Throw-length profiles of faults in this model are similar to those in nature: generally triangular or bell-shaped and often asymmetric and/or with multiple displacement/throw maxima and minima (e.g. Figures 8-10), with the latter indicating position where segments link, commonly via relay ramp breaching (e.g., Huggins et al., 1995, Soliva & Benedicto, 2004; Densmore et al., 2004 for examples of throw-length profiles from outcrop studies, and e.g., Walsh et al., 2003; Nicol et al., 2005; Jackson et al., 2013, 2017; Ze & Alves, 2019; Lathrop et al., 2021 for examples of throw-length profiles derived from 3D seismic reflection studies). Modelled faults also follow a broadly similar growth pattern to those identified in natural systems; at the array scale, faults experience a relatively brief period of lengthening, followed by a more protracted period of throw accumulation (e.g., Walsh et al., 2002, 2003; Nicol et al., 2005; Jackson & Rotevatn, 2013; Henstra et al., 2015; Fossen & Rotevatn, 2016; Hemelsdaël & Ford, 2016; Tvedt et al., 2016; Childs et al., 2017; Jackson et al., 2017; Rotevatn et al., 2019). Fault growth will be detained in detail later in the discussion (section 4.3).

We use the same apparatus as Zwaan et al., (2016; 2019; 2020; 2021a, b), however our study differs from those previous models because it does not use a seed to initiate faulting. Models with seeds form one main rift along the length of the seed, which is ideal for studying topics such as rift interaction and rift basin propagation, whereas our model set-up allows for a more distributed fault network to develop, which is more suited to a more detailed analysis of the growth of individual segmented faults and their host networks.

Despite differences in modelling approach, our results are consistent with previous sandbox analogue studies that measured fault throw and length through time (see Schlagenhauf et al., 2008; Wang et al., 2021; Schmid et al., 2022a; Mayolle et al., 2023). Schlagenhauf et al. (2008) document a hybrid style of fault growth, characterised by an initial period of rapid lengthening (around one-third of the model duration), followed by a stage of displacement accrual, during which time little or no lengthening occurs, and that persists for the remainder of the model. They theorize that faults have cyclical growth patterns and state that faults cannot have a D/L>1, such that once a fault approaches that ratio, it will lengthen via segment linkage and return to a period of displacement accrual (Schlagenhauf et al., 2008). Our high-resolution models confirm their hypothesis and in fact, captures multiple stages of this cyclical growth (Figure 11). The set-up and analysis of Schlagenhauf et al. (2008) had two major differences to our model. First, foam wis compressed and extended only in the middle of their model, which results in uneven extension across the length of the model and somewhat unrealistic, curvilinear faults (Schlagenhauf et al., 2008). In contrast, extension is uniformly distributed, and faults remain relatively straight across the length of our model (Figure 2). Second, Schlagenhauf et al. (2008) tracks displacement and length with an overhead laser tracker, whereas we use 3D CT scans to in order to visualise fault interactions at depth.

Wang et al. (2021) model fault reactivation in response to non-coaxial extension, finding that reactivated faults follow a constant-length model, whereas non-reactivated (i.e. ‘new’) faults follow a propagating fault model. Faults are measured twice (at 2 and 3 cm of extension); between those time steps, fault displacement increases, and the faults link with adjacent segments (Wang et al., 2021). Wang et al. (2021) consider that these faults grow via the propagating growth model. However, we speculate that this could simply be one phase of cyclical growth as shown in our model, suggesting that if growth was tracked at higher resolution or if extension was to continue, faults would likely experience a more protracted stage of post-linkage throw accrual.

No matter how closely spaced synthetic faults are our models, all faults have a constant dip of ~64˚ and thus do not form vertically branching or listric faults as seen in nature (e.g., Soliva et al., 2008). The reason that fault dip does not change could be due: 1) in our model, extension being induced by the expanding foam at the bottom of the model, but in nature it could be induced by forces acting from the side of the system as well, so this could cause our faults to behave differently; 2) during the early stages of extension (pre-20 mm), the faults are too closely spaced together to allow for later changes in dip, or; and 3) changes in fault dip may require us to use models with thicker sand layers or additional extension.

4.2. Strain Localisation

As fault networks evolve, strain is partitioned onto fewer, optimally positioned faults (e.g., Cowie, 1998; Gawthorpe & Leeder, 2000; Cowie & Roberts, 2001; Pan et al., 2021). Strain localisation is also seen in our models, with numerous short, low-throw, very closely spaced faults characterising the initial stages of extension, and fewer, longer, larger-throw, more widely spaced faults defining the latter stages of extension (Figure 6). Throughout extension, strain progressively becomes more localised, and the amount of strain on each fault becomes more varied. Specifically, between 6 mm and 38 mm of extension, the average spacing between faults increases from ~1.1 mm to ~0.6 mm and the total number of active faults decrease by 36%, with the bulk of strain across the width of the model only being accommodated by four faults at the end of the model (Figures 6a and 6e). During extension, faults that are optimally positioned (i.e., faults with synthetic boundaries and that are not located in the stress shadows of larger structures) continue to grow via segment linkage, while faults that have conjugate boundaries with adjacent faults and/or that lie in the stress shadows of larger structures become inactive and die (Figure 6). Faults that remain active continue to lengthen via segment linkage to form through-going horsts and grabens across the model that remain active throughout extension.

4.3. Proposed fault growth model

In the fault growth models originally proposed by Cartwright et al. (1996), and further developed by Schlagenhauf et al. (2008), Filbrandt et al. (2007) and Pan et al. (2021), faults follow a cyclical, step-wise growth pattern, alternating between stages of rapid lengthening and slow displacement/throw accrual (Figure 1). This suggests that on individual faults may grow in accordance with the constant-length model, but at the scale of the broader fault array, growth is cyclical. It has been suggested that faults grow in this step-wise manner across all scales, from individual fault segments to entire networks; however, these previous works only capture one stage of fault growth in cm-scale analogue model faults (Filbrandt et al., 2007; Schlagenhauf et al., 2008), numerical simulations (Pan et al., 2022) and km-scale natural normal faults (Pan et al., 2021).

Observations from our analogue model support this cyclical fault growth model, resolving additional stages of step-wise growth (Figure 11). Each step shows a period during which throw accrues, but the fault does not lengthen significantly until two segments physically link. The newly linked fault(s) then return to a period of throw accrual until the next phase of segment linkage. We identify three stages of step-wise growth in F1 and F3, and two stages in F2 (Figure 11). The exception to this growth pattern is the increase in length in F1 from 22 mm to 24 mm of extension, although this is likely partially due to throw being too low to clearly delineate the full fault length after 22 mm extension (Figure 8a).

During the earliest stages of extension, short, isolated, closely-spaced, low-throw fault segments developed and begin to accumulate throw while maintaining a relatively stable length (Figure 12a1). The tips of the fault segments then propagate enough to interact and link with adjacent synthetic fault segments, increasing their length dramatically (Figure 12a2). These fault arrays then maintain a relatively stable length with small amounts of tip propagation (mm scale in our model) while accruing throw (Figure 12a3). Faults with conjugate boundaries and faults in stress shadows do not lengthen and will eventually become inactive as strain is localised onto the larger, optimally spaced faults (Figure 12a3). Active faults across a larger scale (Figure 12b1) will then propagate a small amount until they interact and link with adjacent synthetic faults, dramatically increasing their total length again (Figure 12b2). The newly linked faults then maintain a relatively stable length with some (mm scale in our model) tip propagation whilst accruing throw. In theory, this pattern will continue until either 1) extension stops, or 2) the fault encounters a barrier that prevents further segment linkage, such as a conjugate boundary with an adjacent fault, or 3) the fault becomes inactive due to stress being partitioned onto a more optimally situated fault. This could be tested in the future through analogue modelling with increased extension (i.e., >4 cm extension) as well as through numerical modelling.

Fault segments with conjugate boundaries with adjacent segments are prevented from growing laterally. In our models, the northern tip of F1 and both the northern and southern tips of F3 have conjugate segments boundaries with adjacent structures. Fault segments become pinned relatively early, which restricts further fault growth via segment linkage or tip propagation. For example, the northern tip of F1A is pinned by a conjugate fault by 28 mm of extension, which prevent it from growing laterally for the rest of extension (Figure 8). This is likely one of the reasons that faults stop lengthening quickly; once faults start to grow laterally and interact with a conjugate fault, they are mechanically blocked from lengthening any further; this process is common across the model and in natural examples (e.g., Moriya et al., 2005; Pan et al., 2021).

5. Conclusion

We use an innovative analogue modelling approach to study normal fault growth by tracking fault lengthening and throw accumulation in 3D and through time. We have found the following:

- Strain is increasingly localised onto fewer, larger faults through time. Faults with synthetic boundaries (i.e., segments that approach each other along strike and dip in the same direction) will remain active, and faults in stress shadows or with conjugate boundaries (i.e., segments that approach each other along strike and dip in the opposing direct) will become inactive early and strain is partitioned onto larger faults.

- Overall, faults show a step-wise growth pattern with alternating stages of lengthening and throw. Fault segments lengthen via segment linkage by interacting with adjacent fault segments and then remain at a constant length (with some minor tip propagation) while accumulating throw. Faults will again have another stage of lengthening via linking with an adjacent synthetic fault segment, and then remain at that length while accumulating throw. This cyclical growth continues until the fault either becomes inactive due to strain being localised onto another nearby fault or until extension ends.
- This mechanism of cyclical fault growth has been suggested before (Cartwright et al., 1996; Filbrandt et al., 2007; Schlagenhauf et al., 2008; Pan et al., 2021), but this is the first time that several stages of cyclical fault growth have been directly observed.
- These model results improve our overall understanding of fault kinematics and fault growth from the segment to the network scale and has implications in potential seismic hazards.

Supplementary Section

We completed a total of four rifting models with different configurations and extension velocities for our study, but the analysis presented in this paper was completed on the most geometrically realistic model (i.e., the model with the configuration that allowed horsts and grabens to form and strain to be partitioned). Information on the additional models as well as additional figures from every stage of extension can be found in the supplementary material.

Acknowledgements

The physical analogue modelling carried out in this paper was conducted at the University of Bern, Switzerland. We thank the AAPG for providing a Grain-In-Aid grant which was used to carry out this research. We thank the Geologists' Association for providing a New Researchers grant from the Wiley Fund which was used to carry out this research. We thank Imperial College for providing B. Lathrop with the Presidential scholarship to fund their PhD research, and the Swiss National Science Foundation for financing F. Zwaan and T. C. Schmid (grant 200021-178731, http://p3.snf.ch/Project-178731). F. Zwaan is also supported by a GFZ Discovery Fund fellowship. We thank Nicole Schwendener for her help with the CT-scanning. We also thank Jean-Marie Mengus (IFP Energies Nouvelles) for converting our CT scan files to .SGY files. We thank Clare Bond and Alex Whittaker for providing feedback and corrections to this research as B. Lathrop's PhD examiners.

Author contributions

Conceptualization: B. Lathrop, F. Zwaan, C. Jackson, R. Bell, A. Rotevatn

Modelling: B. Lathrop, F. Zwaan, T. Schmid, G. Schreurs

Data Analysis: B. Lathrop, T. Schmid

Funding acquisition: B. Lathrop, F. Zwaan, G. Schreurs, C. Jackson, R. Bell, A. Rotevatn

Supervision: C. Jackson and R. Bell were the supervisors of B. Lathrop's PhD work. G Schreurs is the supervisor of the Bern Laboratory Facilities.

Writing: original draft: B. Lathrop

Writing: review and editing: All authors

Figures

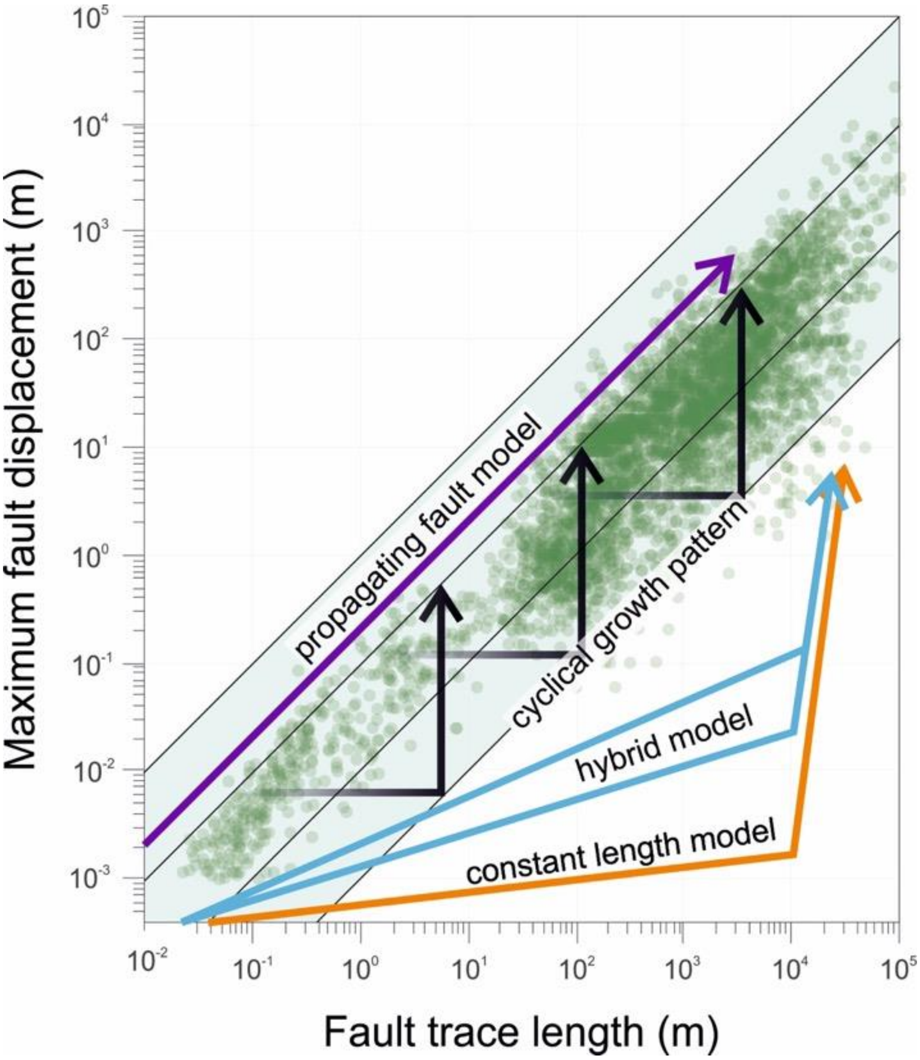

***Figure* 1.** *Global displacement-length (D-L) database from Lathrop et al., 2022 (see sources therein). Fault growth trajectories of the constant-length model (e.g., Walsh et al., 2002, 2003; Nicol et al., 2005; Jackson & Rotevatn, 2013; Henstra et al., 2015; Fossen & Rotevatn, 2016; Hemelsdaël & Ford, 2016; Tvedt et al., 2016; Childs et al., 2017), the hybrid model (e.g., Jackson et al., 2017; Rotevatn et al., 2019), the propagating fault model (e.g., Morley et al., 1990; Dawers et al., 1993; Cartwright et al., 1995; Walsh et al., 2003), and cyclical fault growth model (Cartwright et al., 1996; Filbrandt et al., 2007; Schlagenhauf et al., 2008; Pan et al., 2021) are shown.*

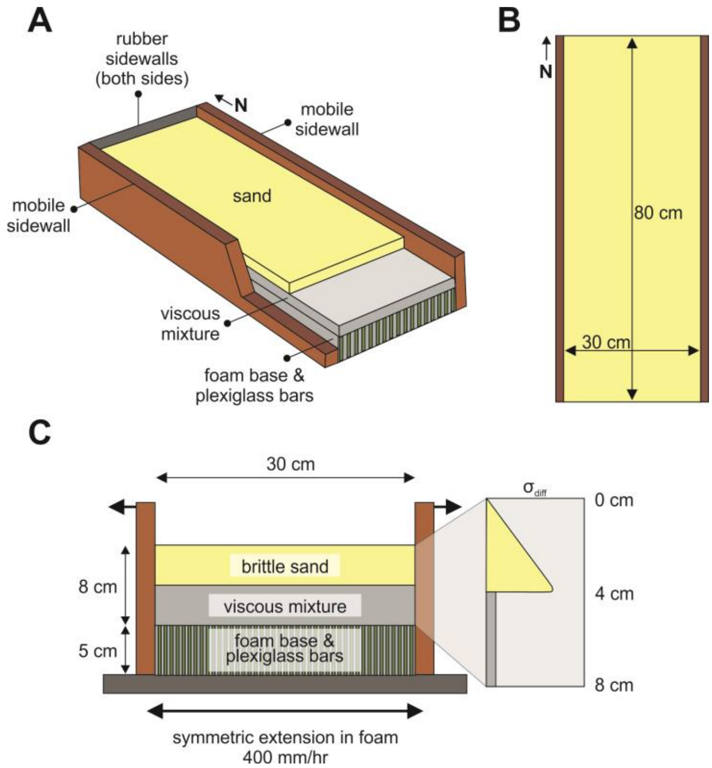

Figure 2. *Model set-up. A) 3D set-up of the model. B) Top view of the model. C) Cross-section view of the model with a schematic of the strength profile for viscous-brittle setup. 'North' has been assigned in A and B. Modified after Zwaan et al., 2020.*

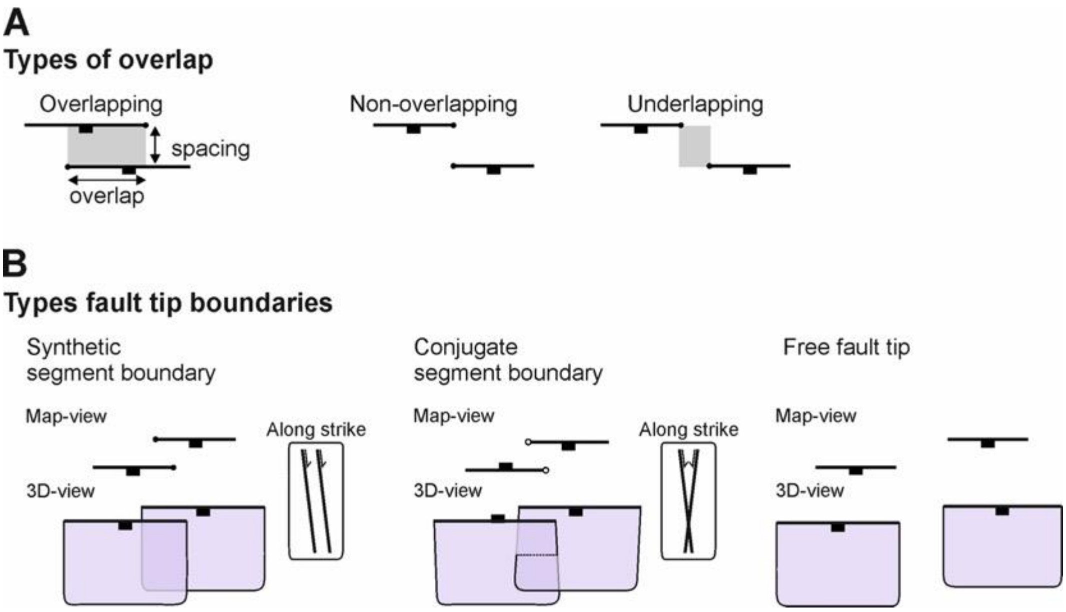

Figure 3. *Outline of fault overlap geometries. A) Types of lateral fault tip overlap including overlapping, non-overlapping, and underlapping. B) Types of fault tip boundaries including synthetic segment boundaries, conjugate segment boundaries, and free fault tips, shown in map-view, 3D-view and along strike (see Trudgill & Cartwright, 1994; Cartwright et al., 1995; Whipp et al., 2016).*

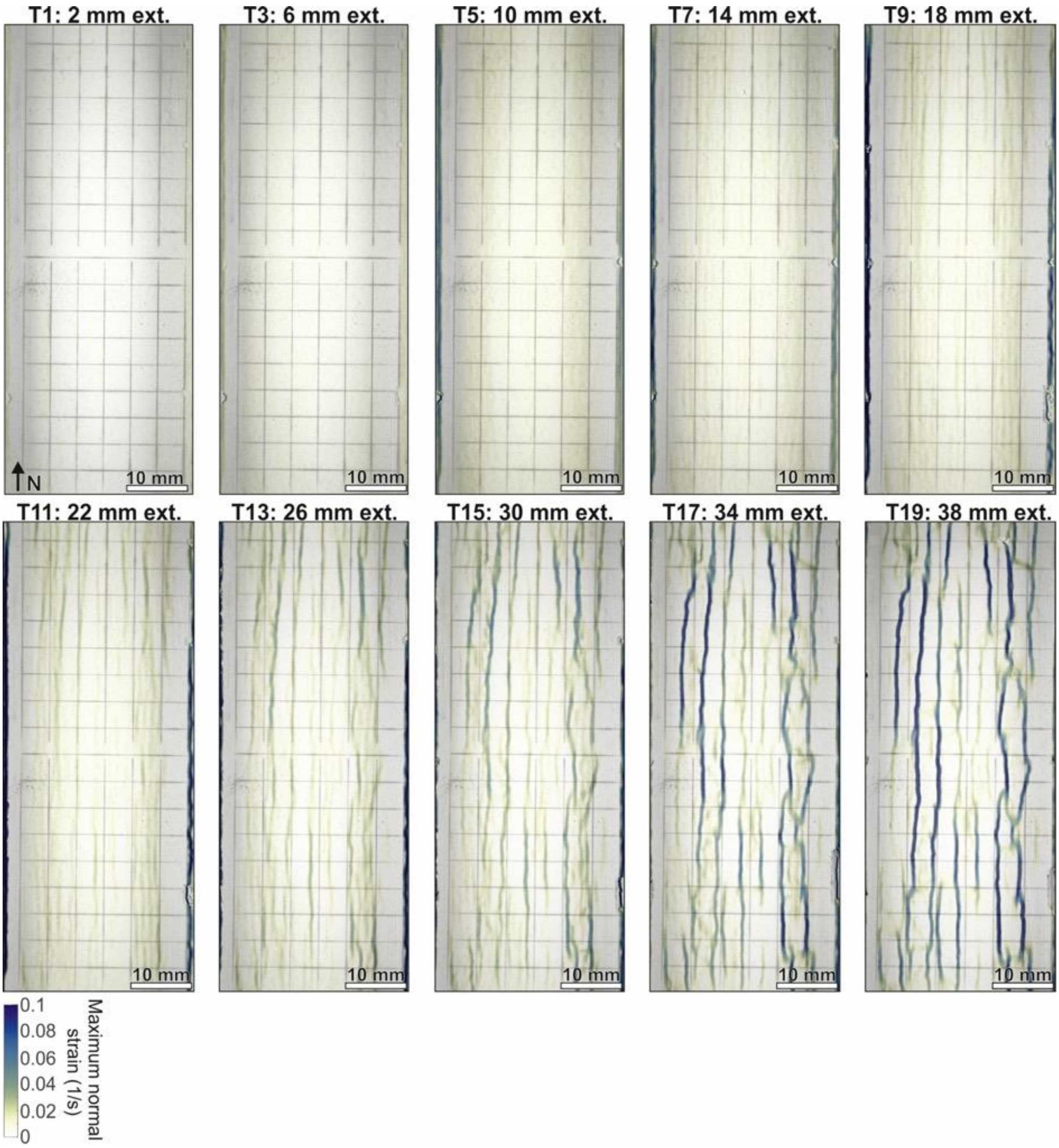

Figure 4. *Top-view results from surface DIC analysis of at every 4 mm of extension. Some faulting can be seen at ~6-8 mm extension. North direction is labelled in T1 and is the same throughout. There was an error with overhead imaging at 40 mm ext., and thus is not shown. Scans were taken at every 2 mm of extension and all of the images can be found as Supplementary Figures 6 and 7.*

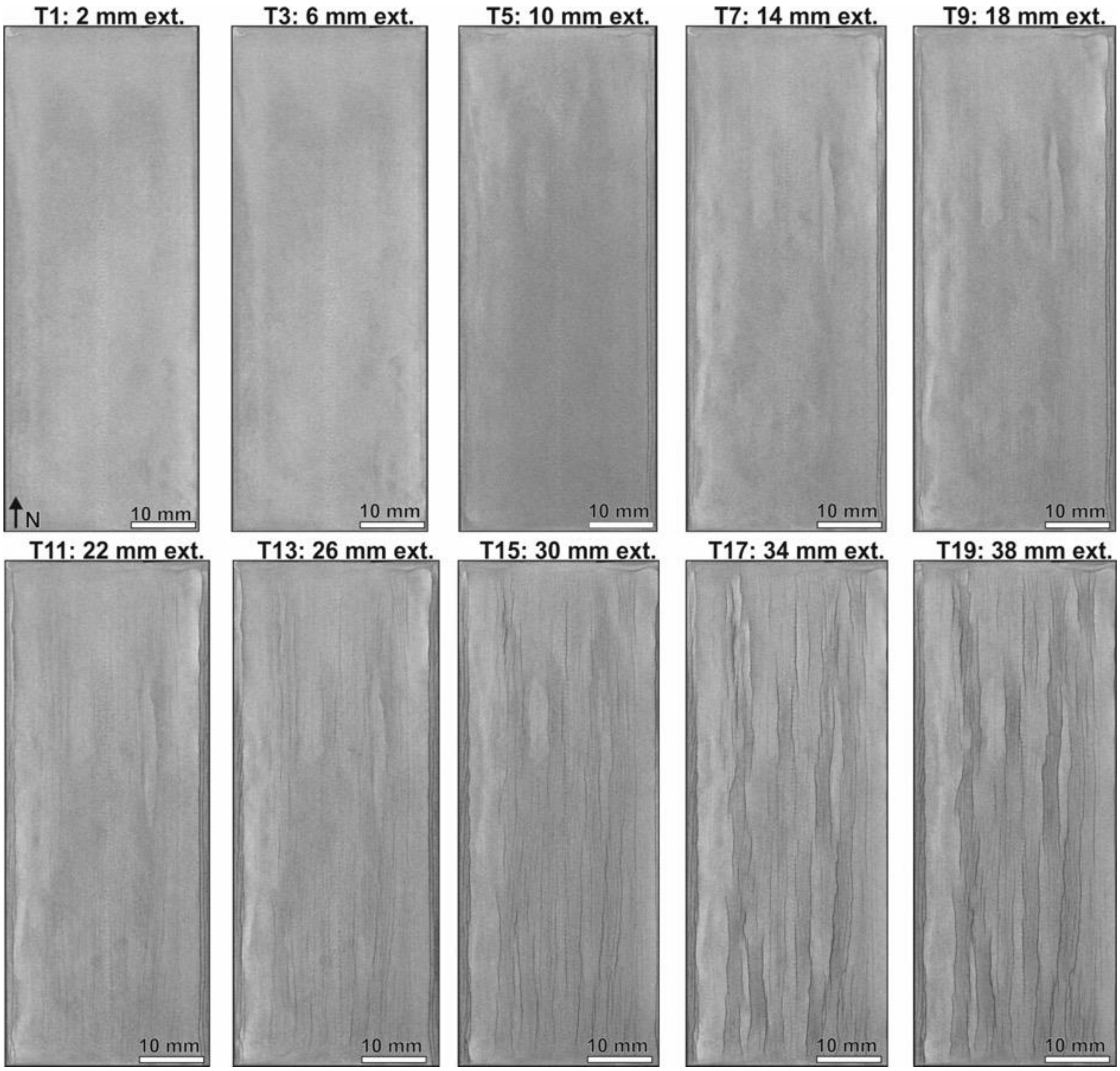

Figure 5. *CT scan images at every 4 mm of extension model. Images are showing the upper part of the model (~0.5 cm from the model surface). Some faulting can be seen at ~10 mm extension. North direction is labelled in T1 and is the same throughout. Scans were taken at every 2 mm of extension and all of the images can be found as Supplementary Figure 8 and 9.*

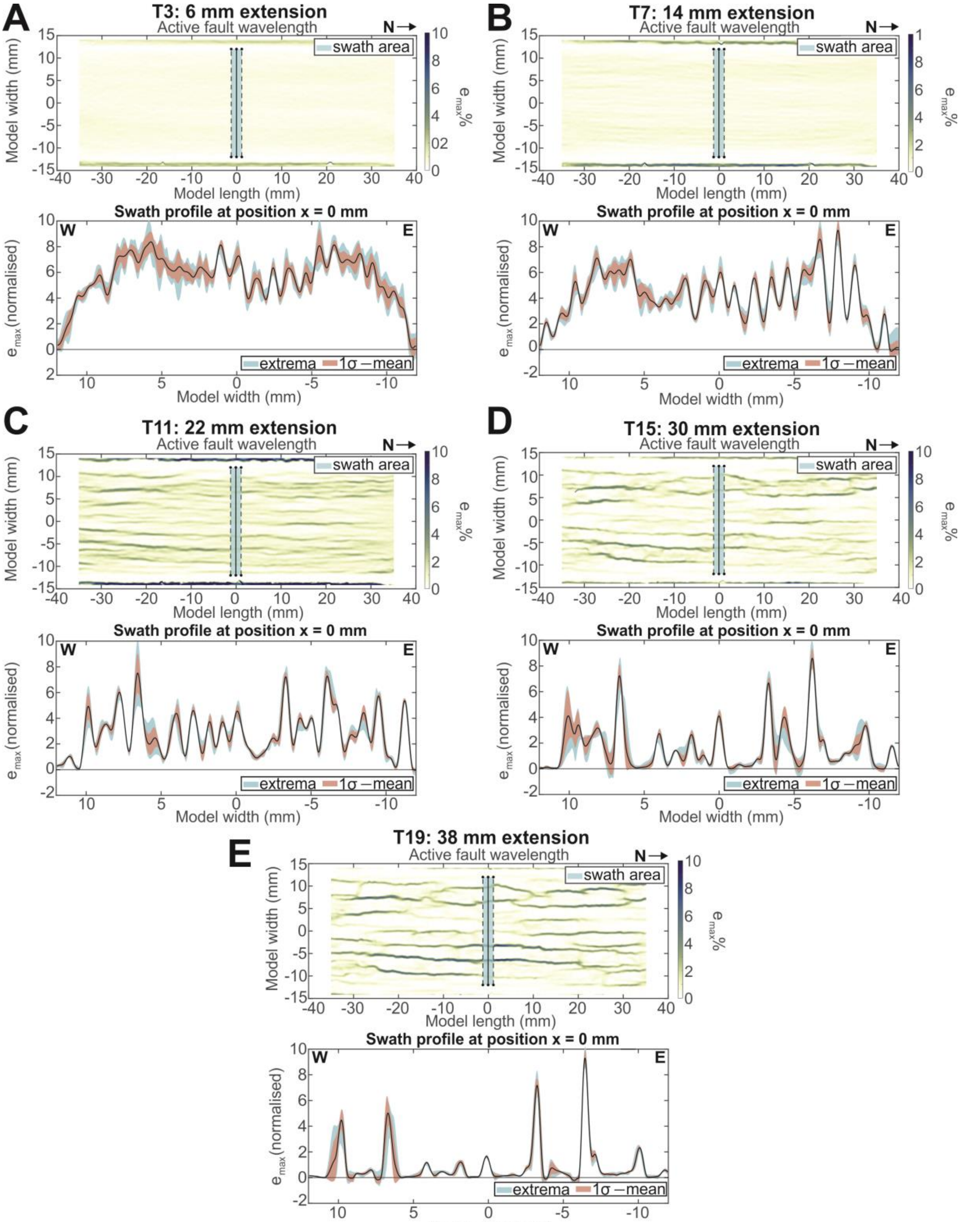

Figure 6. Swath profiles showing e_{max} (incremental maximum normal strain) to indicate active fault wavelength. e_{max} is normalised using the maximum occurring e_{max} value for better comparison. Profiles are shown at A) 6 mm extension, B) 14 mm extension, C) 22 mm extension, D) 30 mm extension, and E) 38 mm extension. Each local maximum in the profiles indicates an active fault. The swath profiles are taken at x=0 mm and have a width of 2 mm. Solid black lines indicate the swath profiles' mean value. Dark and light blue areas indicate the 1 standard deviation and extrema, respectively. Active fault wavelength for every 2 mm of extension can be found in Supplementary Figure 10-13.

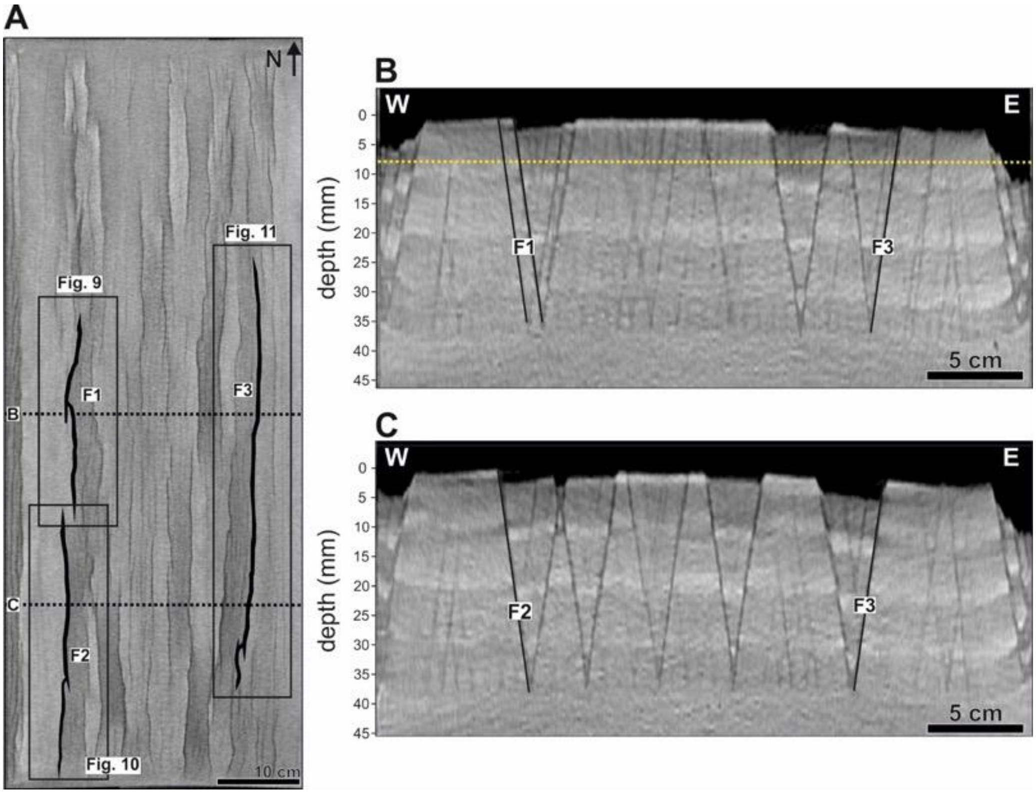

Figure 7. *Overview and cross-section of model. A) Overhead view of model at 40 mm extension, showing the overall structures of the model. Fault 1 (F1), Fault 2 (F2), and Fault 3 (F3) are labelled. Depth of image is shown in figure B with the black dashed line. B) W-E cross-section view through F1 and F3. Location of cross section is labelled in panel A with a black dashed line. C) W-E cross-section view through F2 and F3. Location of cross section is labelled in panel A with a black dashed line. The cross-sections have a vertical exaggeration of 1:3.*

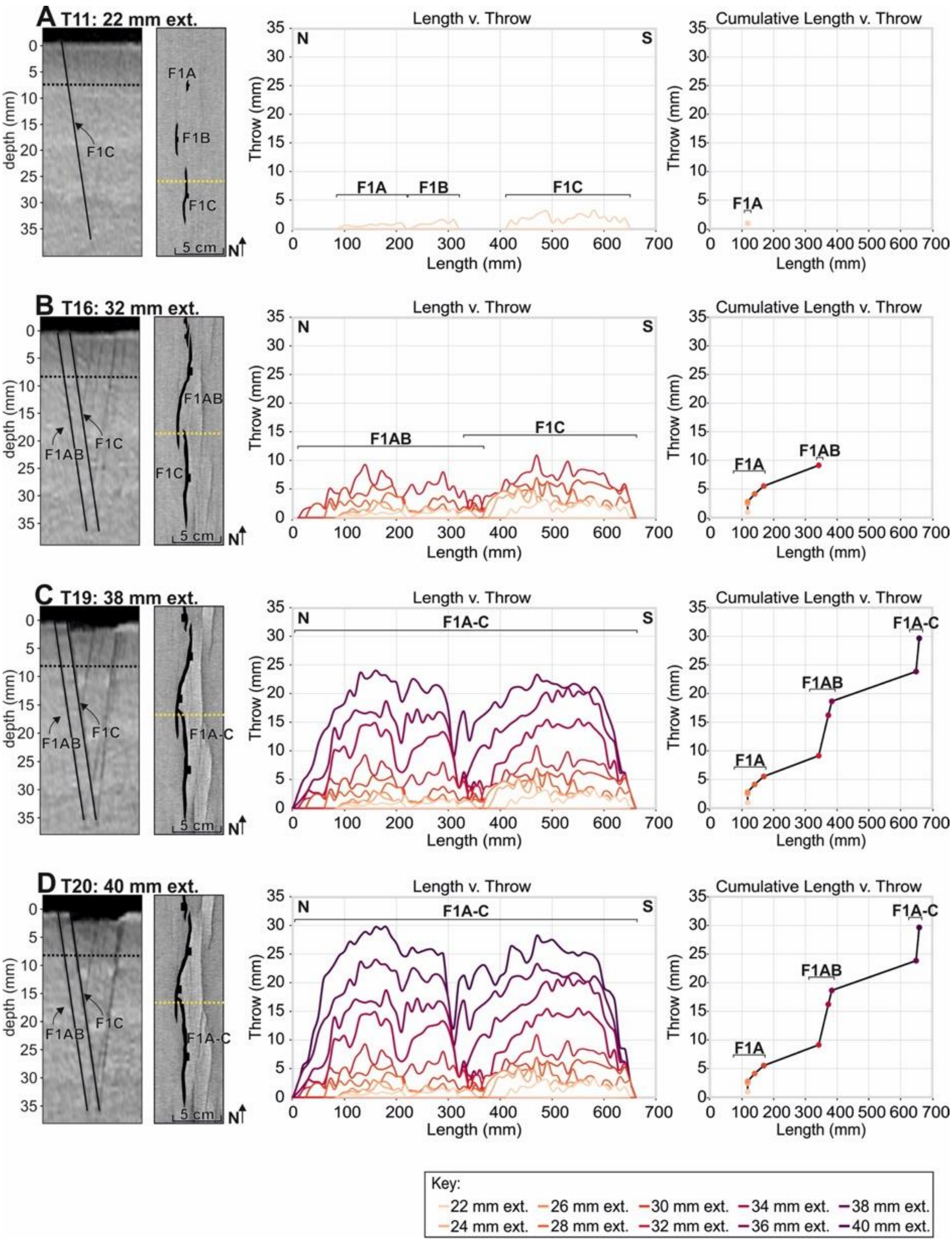

Figure 8. *Figure showing the fault length, throw, and segment linkage for Fault 1 at A) 22 mm extension, B) 32 mm extension, C) 38 mm extension, and D) 40 mm extension. These intervals were chosen to show the start of the analysis (22 mm ext.), the points of fault segment linkage (32 and 38 mm ext.), and the end of analysis (40 mm ext.). Faults are shown in cross-section and overhead view with F1A-C labelled, along with throw-length plots and a cumulative throw-length through time at every 2mm ext. The locations of the cross-sections are indicated by the yellow dashed line on the overhead image. Measurements of fault length and throw are taken at these depths. The location of Fault 1 is labelled in figure 7. Cross-sections*

have a vertical exaggeration of 1:3. Cross-section and map-view images at every 2 mm extension (22-30 mm) can be found in Supplementary Figure 14.

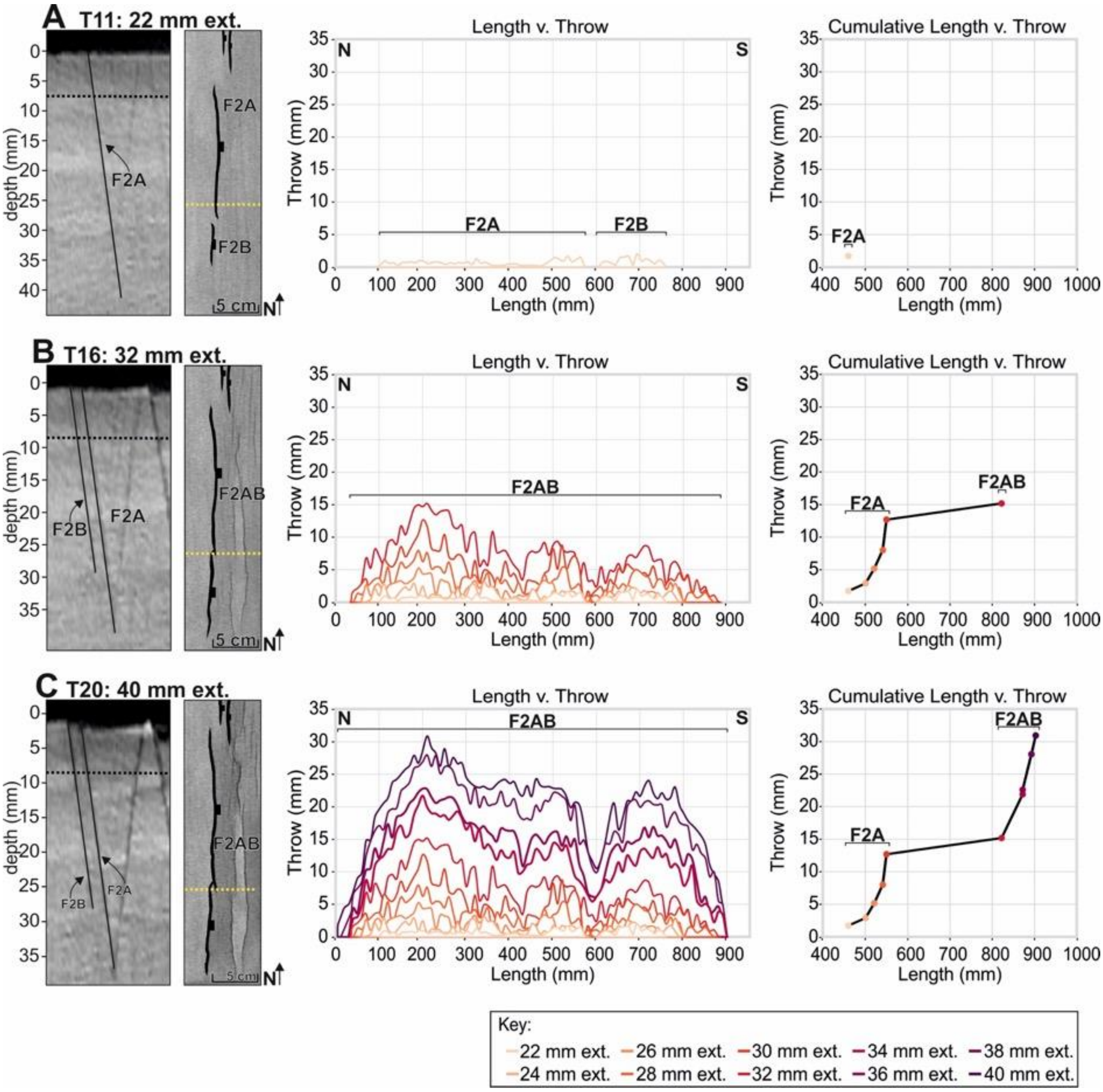

Figure 9. *Figure showing the fault length, throw, and segment linkage for Fault 2 at A) 22 mm extension, B) 32 mm extension, and C) 40 mm extension. These intervals were chosen to show the start of the analysis (22 mm ext.), the points of fault segment linkage (32 mm ext.), and the end of analysis (40 mm ext.). Faults are shown in cross-section and overhead view with F2A-B labelled, along with throw-length plots and a cumulative throw-length through time at every 2mm ext. The locations of the cross-sections are indicated by the yellow dashed line on the overhead image. Measurements of fault length and throw are taken at these depths. The location of Fault 2 is labelled in figure 7. Cross-sections have a vertical exaggeration of 1:3. Cross-section and map-view images at every 2 mm extension (22-30 mm) can be found in Supplementary Figure 15.*

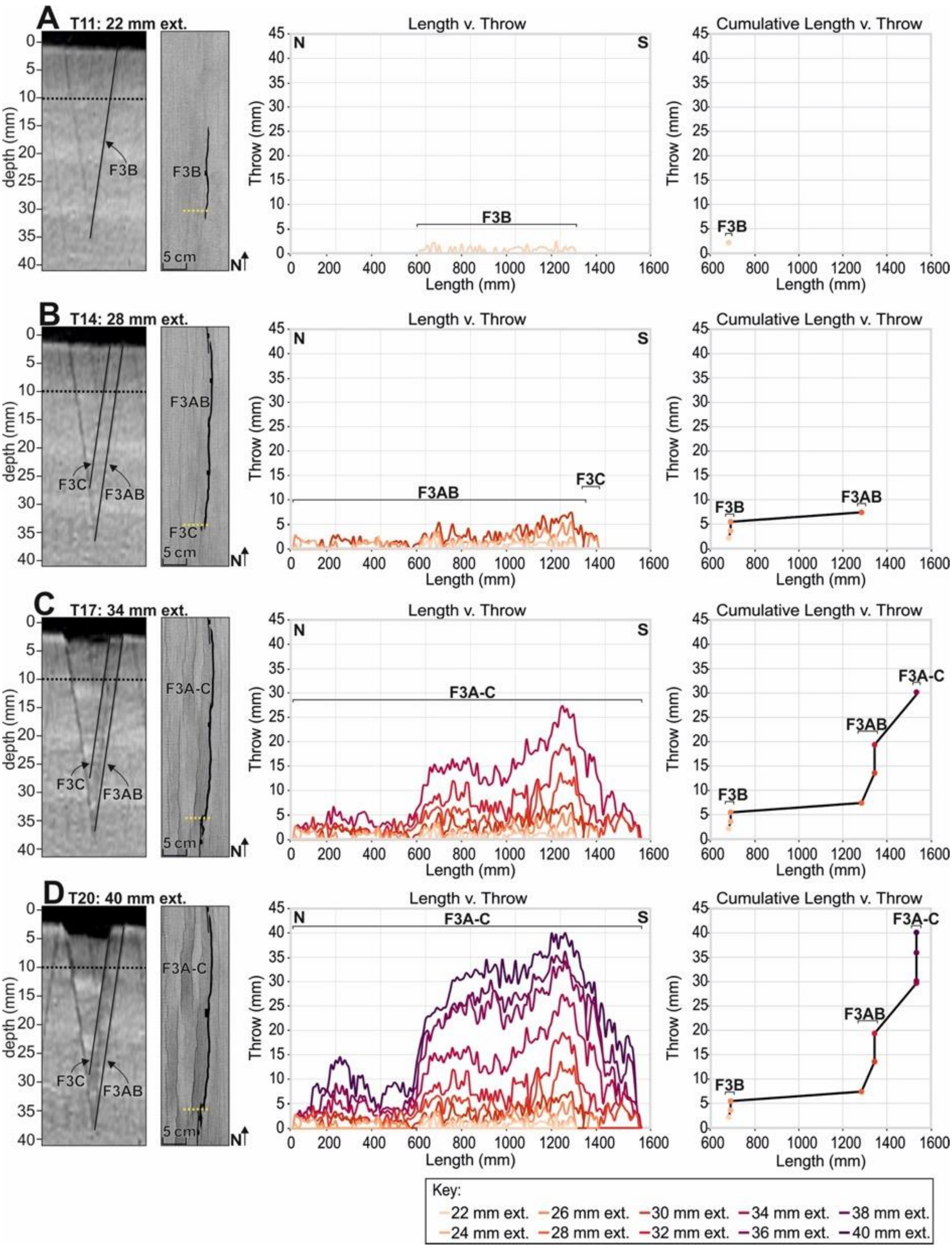

Figure 2. *Figure showing the fault length, throw, and segment linkage for Fault 1 at A) 22 mm extension, B) 28 mm extension, C) 34 mm extension, and D) 40 mm extension. These intervals were chosen to show the start of the analysis (22 mm ext.), the points of fault segment linkage (28 and 34 mm ext.), and the end of analysis (40 mm ext.). Faults are shown in cross-section and overhead view with F3A-C labelled, along with throw-length plots and a cumulative throw-length through time at every 2mm ext. The locations of the cross-sections are indicated by the yellow dashed line on the overhead image. Measurements of fault*

length and throw are taken at these depths. The location of Fault 3 is labelled in figure 7. Cross-sections have a vertical exaggeration of 1:3. Cross-section and map-view images at every 2 mm extension (22-30 mm) can be found in Supplementary Figure 16.

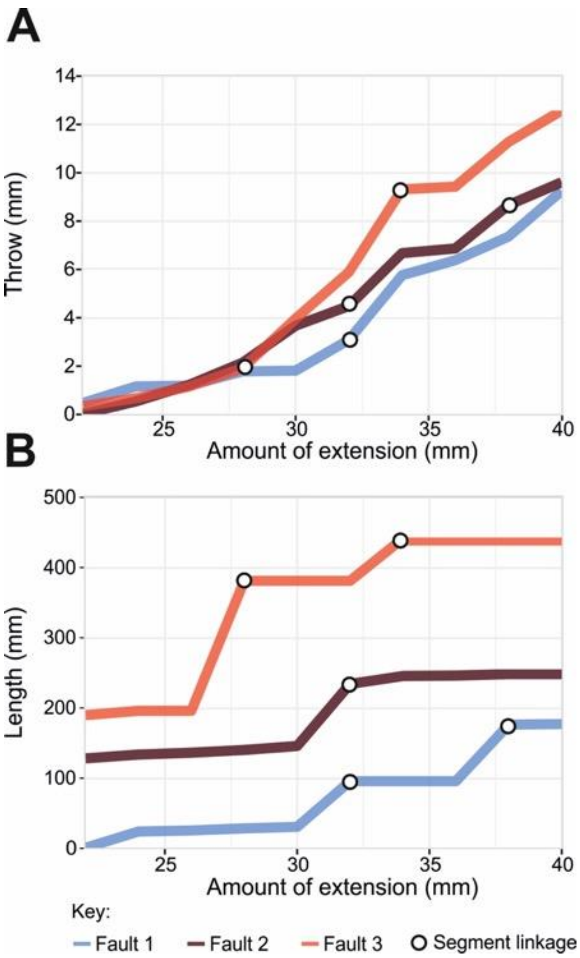

Figure 3. *Figure tracking fault growth through time of Faults 1-3. A) Throw through extension and B) Length through extension. Segment linkage events are indicated with dots.*

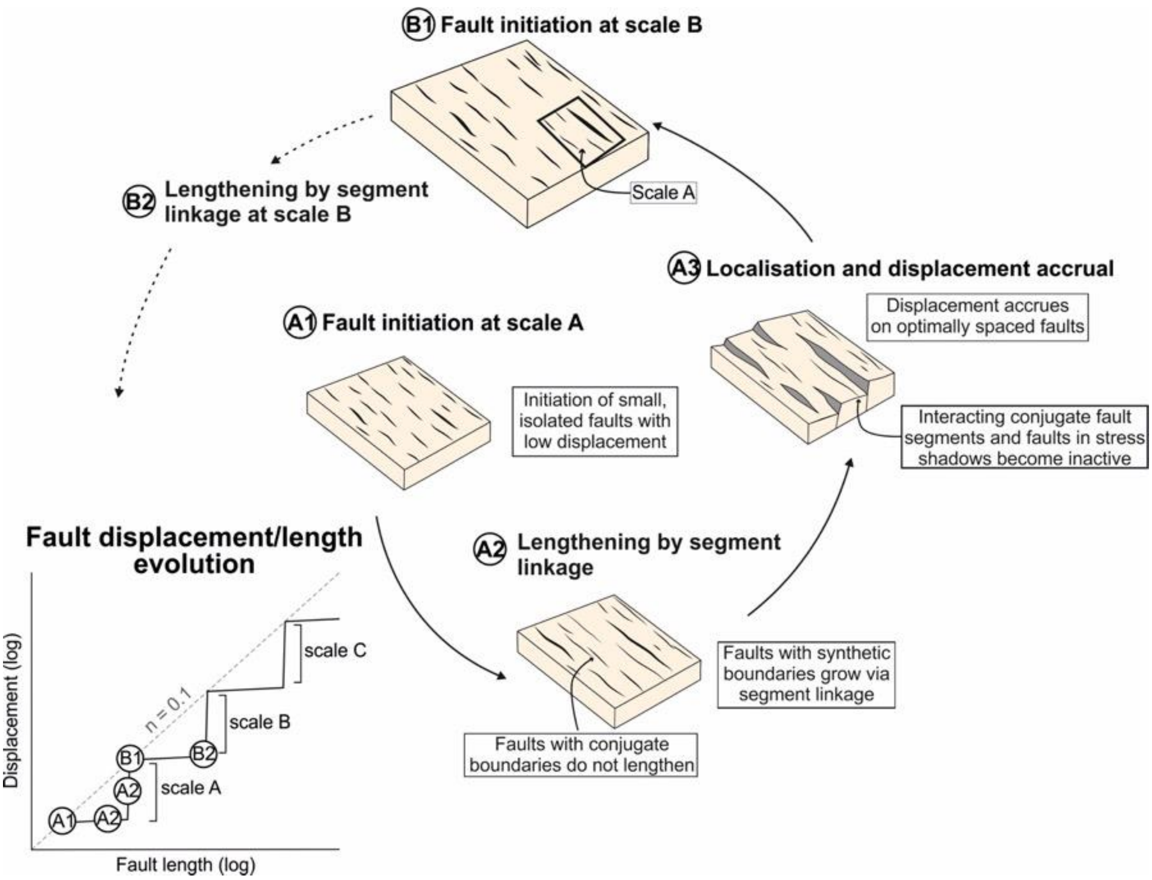

574

575 ***Figure 4.*** *Schematic figure showing cyclical fault growth described in this paper. Cyclical fault growth is*
576 *shown here scales A, B, and C, showing repeating fault growth patterns at the fault segment, array, and*
577 *network scales. A1) Fault initiation at scale A, A2) Lengthening by segment linkage at scale A, A3)*
578 *Localisation and displacement/throw accrual at scale A, B1) Fault initiation at scale B, B2) Lengthening by*
579 *segment linkage at scale B. According to this model, the fault array would then have a period of*
580 *displacement/throw accrual, followed by an initiation and lengthening at scale C. A schematic of these*
581 *steps are labelled on a schematic displacement/length plot on the left. Modified from Pan et al. 2021.*

Material properties			
Granular materials	Quartz sand	Corundum sand	PDMS/corundum mixture
Density (kg/m^3)	1560*	1960*	1600
Grainsize (μm)	60-250	88-175	1 x 10^5
Peak Friction coefficient μ and angle	0.72, 36°	0.78, 38°	1.05
Strain softening (%)	16	18	
Cohesion (Pa)	48±26	55±42	

*Densities with * are achieved by sieving from 30 cm height*

Table 1. *Material properties. Values for quartz sand after Schmid et al. (2020c). Values for PDMS/corundum sand mixture after Zwaan et al. (2016; 2018). Corundum sand values after Panien et. al (2006). Corundum sand values after Panien et. al (2006).*

Appendix

1. Model Scaling

To ensure that our model represented nature, we used standard scaling protocol based on Hubbert (1937) and Ramberg (1981). The stress ratio between the model and nature is defined as:

$$\sigma^* = \sigma_{model}/\sigma_{nature} \quad (1)$$

and the stress ratio is given by the equation:

$$\sigma^* = \rho^* g^* h^* \quad (2),$$

where ρ *, *g**, and *h** represent density, gravity, and length ratios, respectively. Our model yielded a length scaling factor of h^*=2x10^{-6}, a density scaling ratio of ρ^*=5.5x10^{-1} and a gravity scaling ratio of 1, which resulted in a stress ratio of σ^*= 1.1x10^{-6} (Appendix Table 1). Next, the strain rate ratio for viscous materials ε^*= 3.7x10^{10} was calculated with

$$\varepsilon^* = \sigma^*/\eta^* \quad (3)$$

using the stress ratio σ^* and the viscosity scaling ratio η^*= 3x10^{-17} (Appendix Table 1). We used a relatively high lower crustal viscosity, 5x10^{21} Pa s, which has been suggested to be typical for the early stages of magma-poor rifting (e.g., Buck, 1991). The velocity ratio *v** and time ratio *t** were calculated with the equation:

$$\varepsilon^* = \frac{v^*}{h^*} = \frac{1}{t^*} \quad (4)$$

yielding v^*=3.7x10^{10} and t^*=2.7x10^{-11}.

Based on our scaling, 1 cm in our model translates to 5 km in nature, and one-hour correlates to 4.2 Ma in nature. Our model was extended at a rate of 400 mm/hr, which scales to 48 mm/yr in nature. This is fast, but a high extension rate is required to initiate rifting without a seed, and it still aligns with upper limit of the divergence rates compiled by Brune et al. (2016). Our scaling parameters can be found in Appendix Table 1.

To verify dynamic similarity between the brittle layer of our model and the upper crust, we calculated R_s, the ratio between gravitational stress and cohesive strength or cohesion (*C*) (Ramberg, 1981; Mulugeta, 1998):

$$R_s = gravitional\ stress/cohesive\ strength$$

$$R_s = (\rho g h^2)/C \qquad (5)$$

Assuming a cohesion of 12 MPa for rocks in the upper crust and a cohesion of 12 Pa in the sand ($c^*=10^{-6}$), we calculated R_s=51 in both nature and our model. Our assumed cohesion of 12 MPa is relatively low compared to values obtained in rock deformation lab studies (e.g., Handin, 1969; Jaeger and Cook, 1976; Twiss and Moore, 1992), but is reasonable considering that the strength of the crust is generally weakened by multiple phases of deformation. The dynamic similarity between the model's viscous mixture and the lower crust were assessed using the Ramberg number R_m, the ratio between gravitational stress and viscous strength (Weijermars & Schmeling, 1986):

$$R_m = gravitional\ stress/viscous\ strength$$

$$R_m = (\rho g h^2)/(\eta v) \qquad (6)$$

and R_m= 1.5 for both the model and nature. Since R_s and R_m are the same in the model and in nature, we consider our model to be properly scaled and thus a reasonable analogue to continental rifting.

2. Background information on overlapping faults and fault segment interaction

As fault segments grow, they will invariably approach and interact with adjacent fault segments (e.g., Peacock and Sanderson, 1994; Crider and Pollard, 1998; Cowie et al., 2000; Gupta & Scholz, 2000; Fossen & Rotevatn, 2016; Peacock et al., 2016). The development of overlapping lateral fault tips is an important stage of fault growth as it often occurs during fault growth via segment linkage. Fault tips can be described as underlapping, non-overlapping, and overlapping, defined according to their map-view location (Figure 3a) (e.g., Crider & Pollard, 1998; Gupta & Scholz, 2000; Hus et al., 2005; Peacock et al., 2016; Childs et al., 2017). The boundaries between fault segments can be described as either synthetic boundaries, conjugate boundaries, or free tips (Figure 3b). Synthetic boundaries describe interacting fault segments with the same sense of dip direction; depending on how the segments relate to each other spatially, they could interact and link (Figure 3b) (e.g., Morley et al., 1990; Gawthorpe & Hurst, 1993; Childs et al., 1995; Whipp et al., 2016). Conjugate (or antithetic) boundaries describe stepping fault segments with opposite dip directions; these types of fault interactions typically block fault growth by not allowing additional tip propagation or segment linkage (Figure 3b) (e.g., Morley et al., 1990; Gawthorpe & Hurst, 1993; Childs et al., 1995; Whipp et al., 2016). Free tips are fault tips that are not interacting physically or mechanically with another fault and thus are free to propagate laterally (Figure 3b) (e.g., Morley et al., 1990; Gawthorpe & Hurst, 1993; Whipp et al., 2016).

Scaling parameters	Model	Nature
General parameters		
Gravitational acceleration (g)	9.81 m/s^2	9.81 m/s^2
Extension velocity (v)	1.1x10^{-4} m/s	4.3x10^{-10} m/s
Brittle layer		
Material	Quartz sand	Upper crust
Thickness (h)	4x10^{-2} m	2.25x10^4 m
Density (ρ)	1560 kg/m^3	2800 kg/m^3
Cohesion (C)	12 Pa	1.2x10^7 m
Viscous/ductile layer		
Material	PDMS/cor. sand mix	Lower crust
Thickness (h)	4x10^{-2} m	2x10^4 m
Density (ρ)	1600 kg/m^3	3300 kg/m^3
Viscosity (η)	1.5x10^5 Pa s	5x10^{21} Pa s
Dynamic scaling values		
Brittle stress ration (R_s)	51	51
Ramberg number (R_m)	1.5	1.5

Appendix Table 1. *Scaling parameters. Values from model brittle layer from Schmid et al. (2020) and viscous/ductile layer from Zwaan et al. (2018). Values for nature from Corti et al. (2003). Values for PDMS/corundum sand mixture after Zwaan et al. (2016; 2018). Corundum sand values after Panien et. al (2006). Values for nature from Corti et al. (2003).*

Supplementary Material

Rationale for the chosen set-up for analysis

We carried out four different model set-ups inside the CT scanner (supplementary table 1; supplementary figure 1) and we opted to carry out analysis only one model, here referred to as Model A, a brittle-viscous model with a 4 cm sand pack. In the brittle-ductile set-up (Models A and B) we used a foam and plexiglass base because the additional weight of the viscous material would cause a pure foam base to sag. The set-up for Model A can be seen in figure 2 of the main text, and that of Model B is the same as Model A, but with a 6 cm thick sandpack and an extension rate of 800 mm/hr. In the brittle-only set up (Models C and D) the plexiglass base was not needed, so a pure foam base was used and models could have a lower extension rate (8 mm/hr) due to the strain-rate independent rheology of sand (Supplementary Table 1; Supplementary Figure 1).

The ductile layer used in Models A and B allowed strain to be partitioned across the model, which permitted the models to have realistic geological phenomena, such as strain localisation onto larger faults and horst and graben formation (Supplementary Figures 2 and 3). In the brittle-only set up (Models C and D) by contrast, faults were very tightly spaced with more or less equal amounts of displacement across each fault because without a ductile layer, strain had to be accommodated directly above the expanding foam (Supplementary Figures 4 and 5). We chose to conduct our analysis on brittle-ductile Model A, with a 4 cm sandpack (Supplementary Figure 2) as opposed to Model B with a 6 cm sandpack (Supplementary Figure 3) as it was the easiest to track faults in Model A. However, both models would have been acceptable choices.

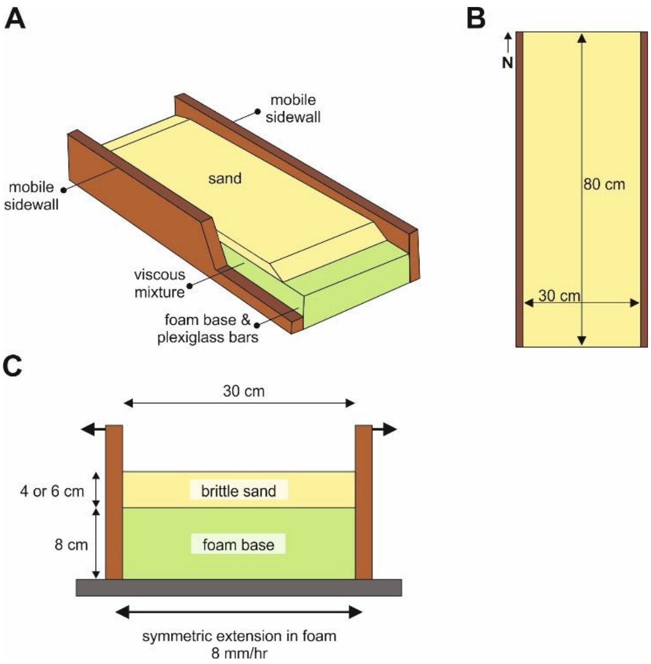

Supplementary figure 1. *Model set-up for brittle-only Models C and D with a pure foam base. A) 3D set-up of the model. B) Top view of the model. C) Cross-section view of the model with a schematic of the strength profile for viscous-brittle setup. Note that Model C had a 4 cm sandpack and Model D had a 6 cm sandpack.*

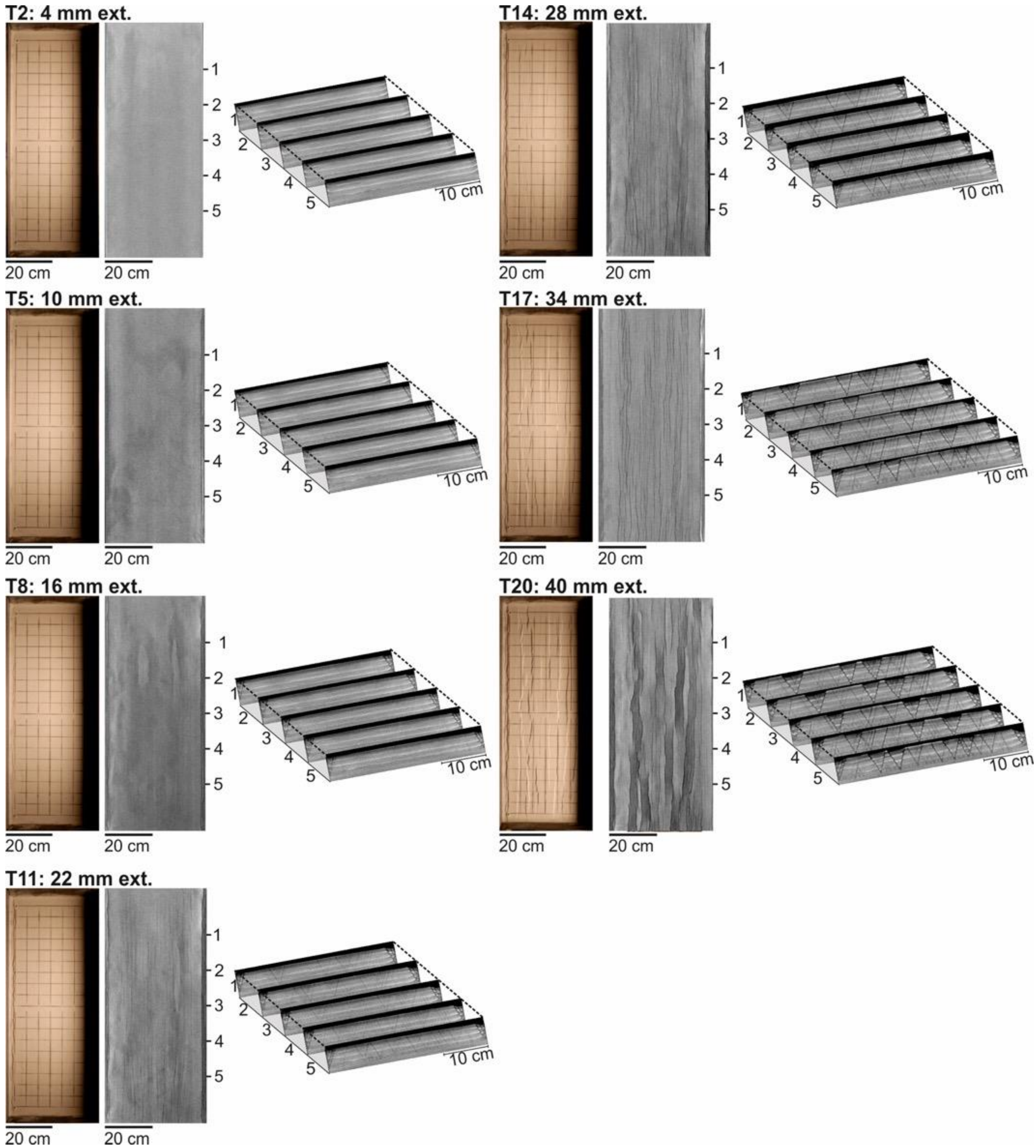

Supplementary figure 2. *Progression of Model A at 4, 10, 16, 22, 28, 34, and 40 mm extension. Photographs of the top view, top of the model in X-Ray view, and cross sections across the model are shown. Locations of each cross-section (labelled as 1-5) are on the top-view images.*

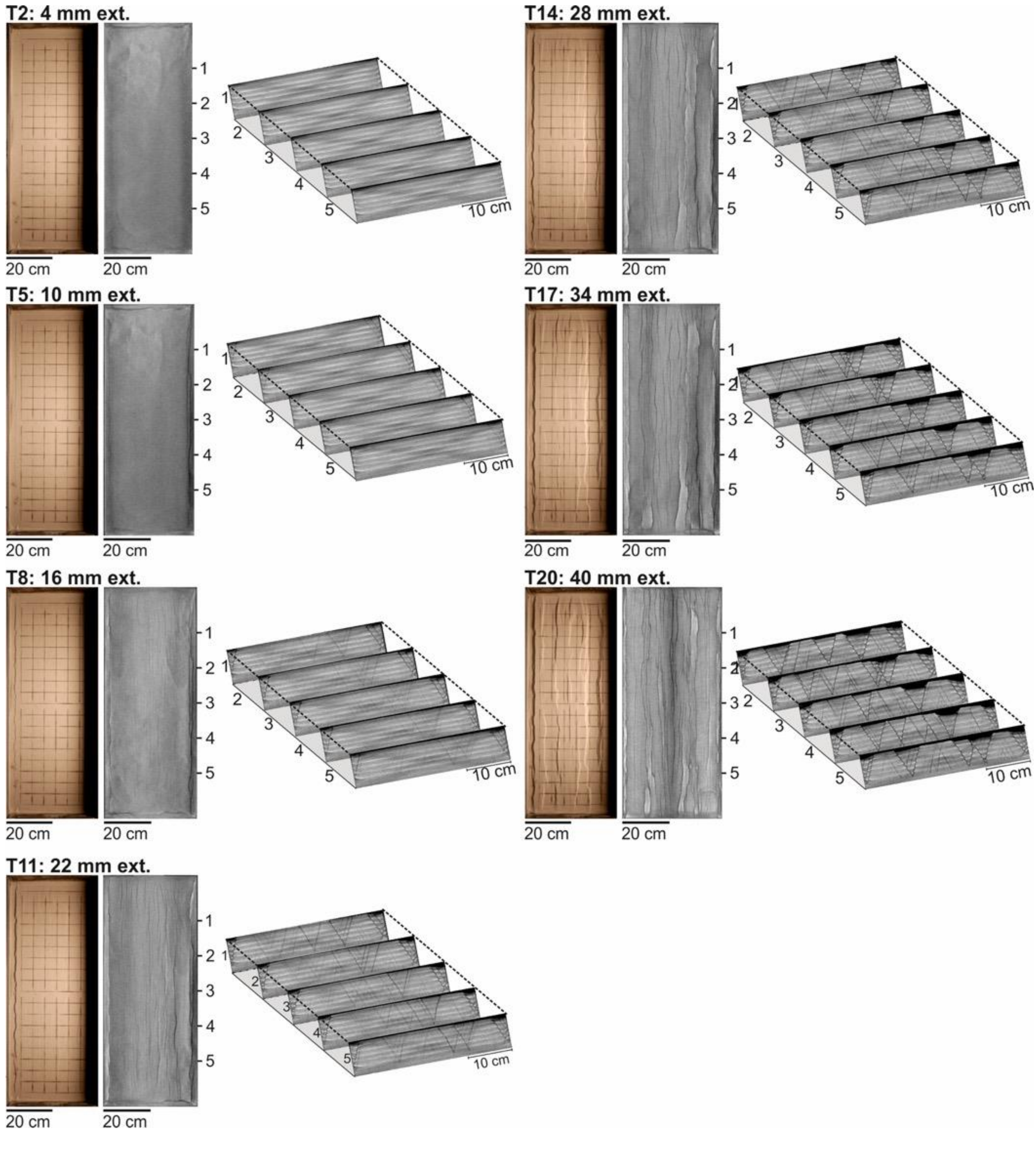

Supplementary figure 3. *Progression of Model B at 4, 10, 16, 22, 28, 34, and 40 mm extension. Photographs of the top view, top of the model in X-Ray view, and cross sections across the model are shown. Locations of each cross-section (labelled as 1-5) are on the top-view images.*

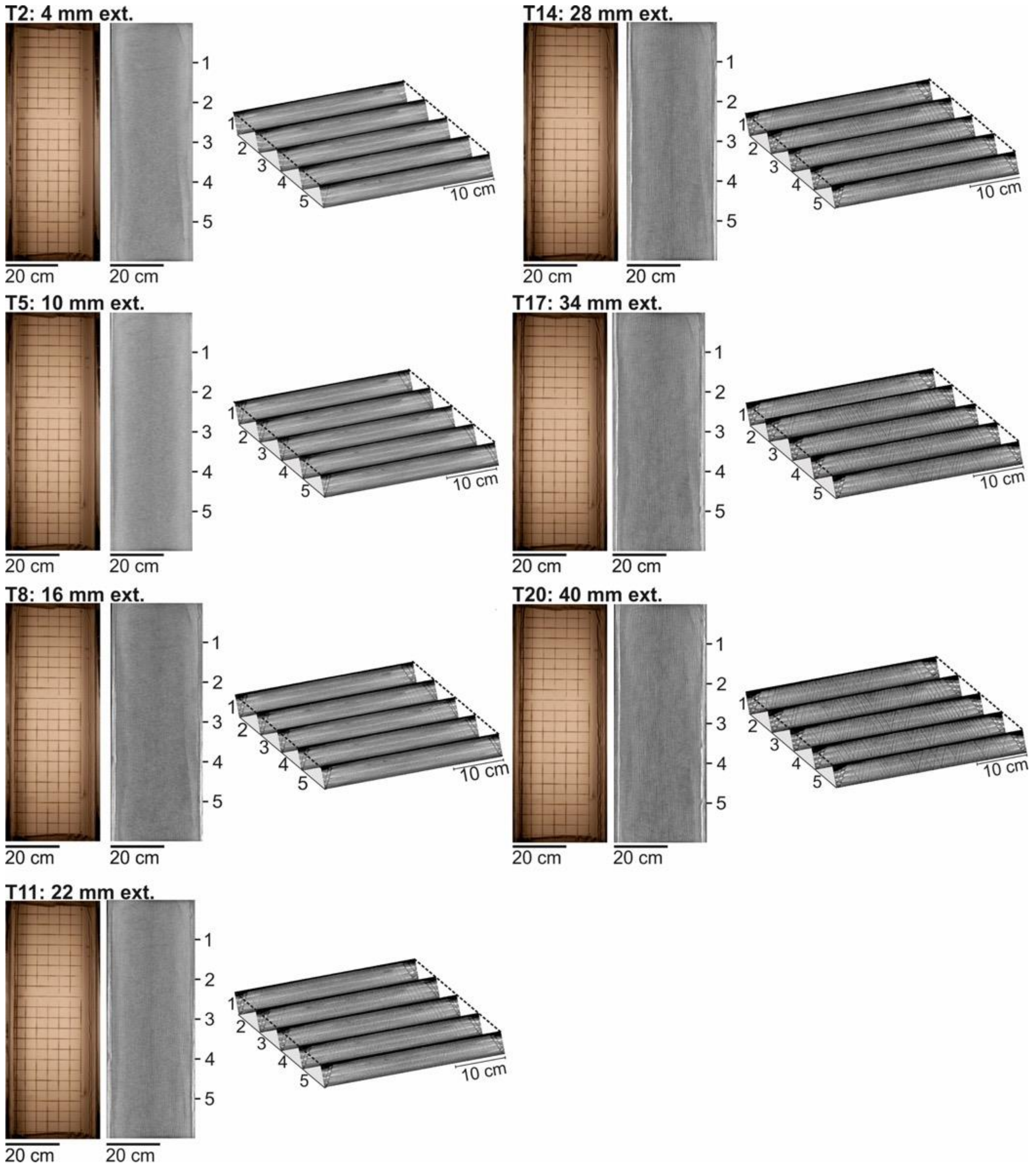

Supplementary figure 4. *Progression of Model C at 4, 10, 16, 22, 28, 34, and 40 mm extension. Photographs of the top view, top of the model in X-Ray view, and cross sections across the model are shown. Locations of each cross-section (labelled as 1-5) are on the top-view images.*

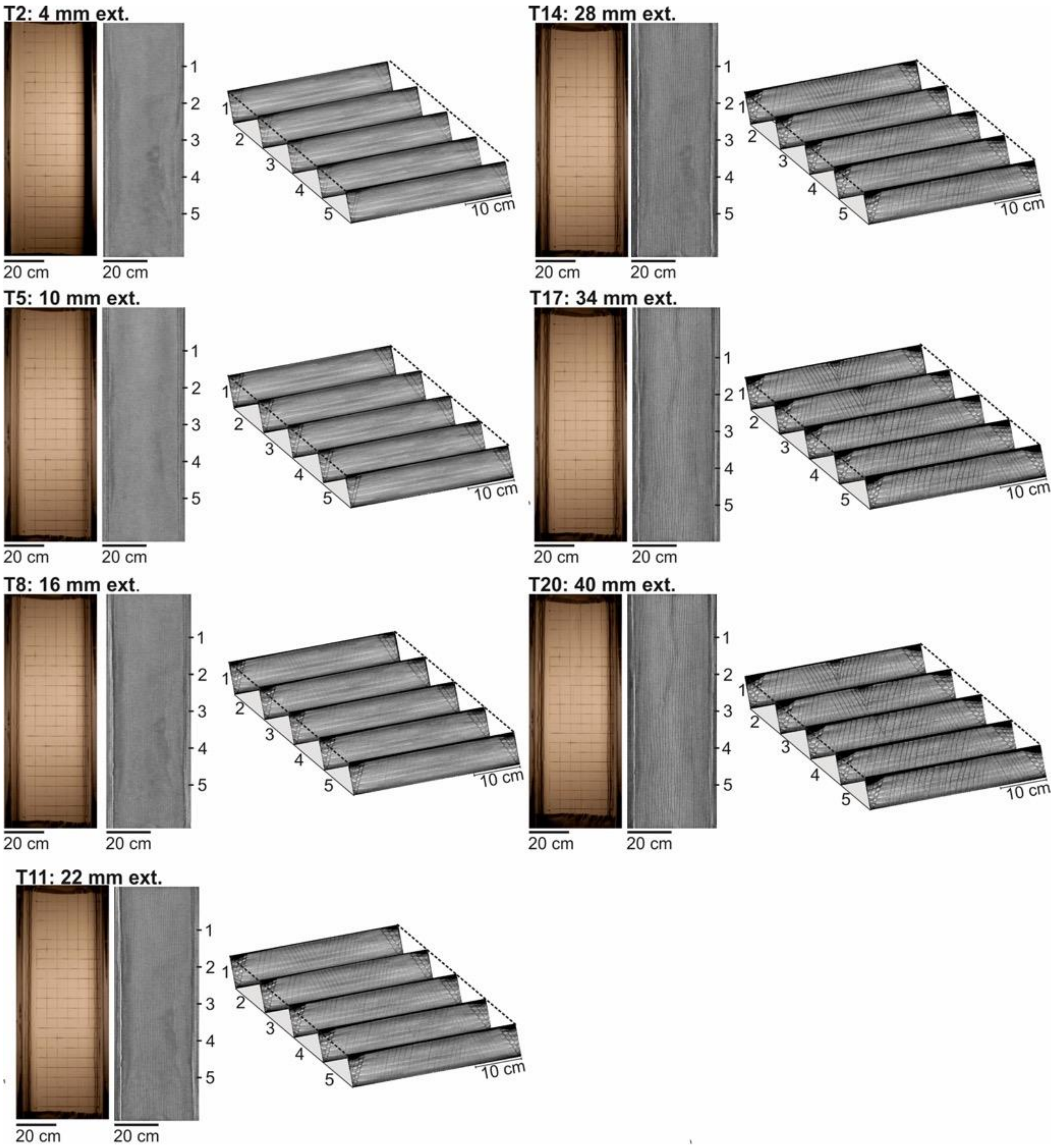

Supplementary figure 5. *Progression of Model D at 4, 10, 16, 22, 28, 34, and 40 mm extension. Photographs of the top view, top of the model in X-Ray view, and cross sections across the model are shown. Locations of each cross-section (labelled as 1-5) are on the top-view images.*

Supplementary figure 6. *Top-view results from surface DIC analysis of at every 2 mm of extension from 2 to 20 mm of extension. North direction is labelled in T1 and is the same throughout.*

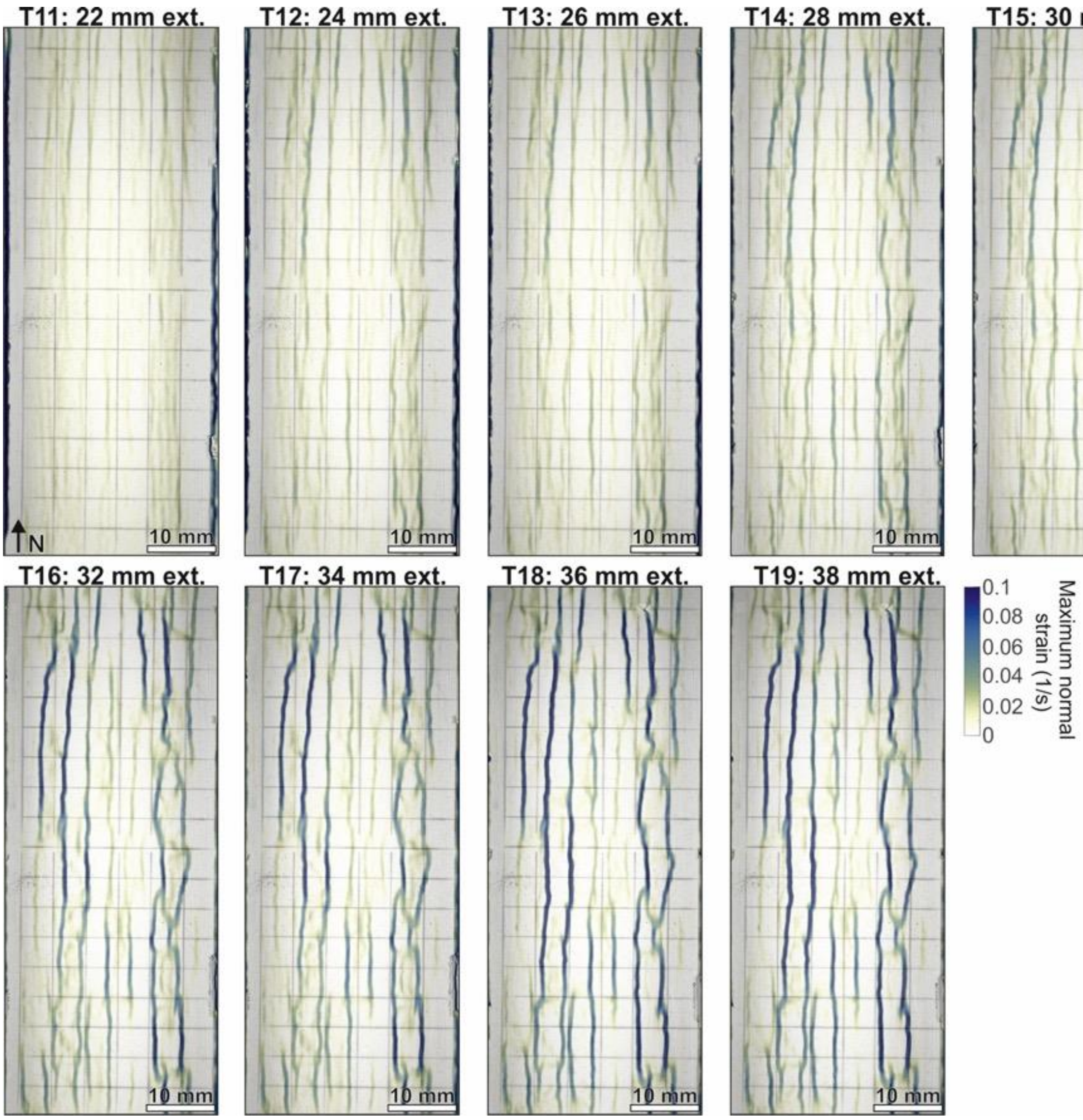

Supplementary figure 7. *Top-view results from surface DIC analysis of at every 2 mm of extension from 22 to 38 mm of extension. North direction is labelled in T11 and is the same throughout.*

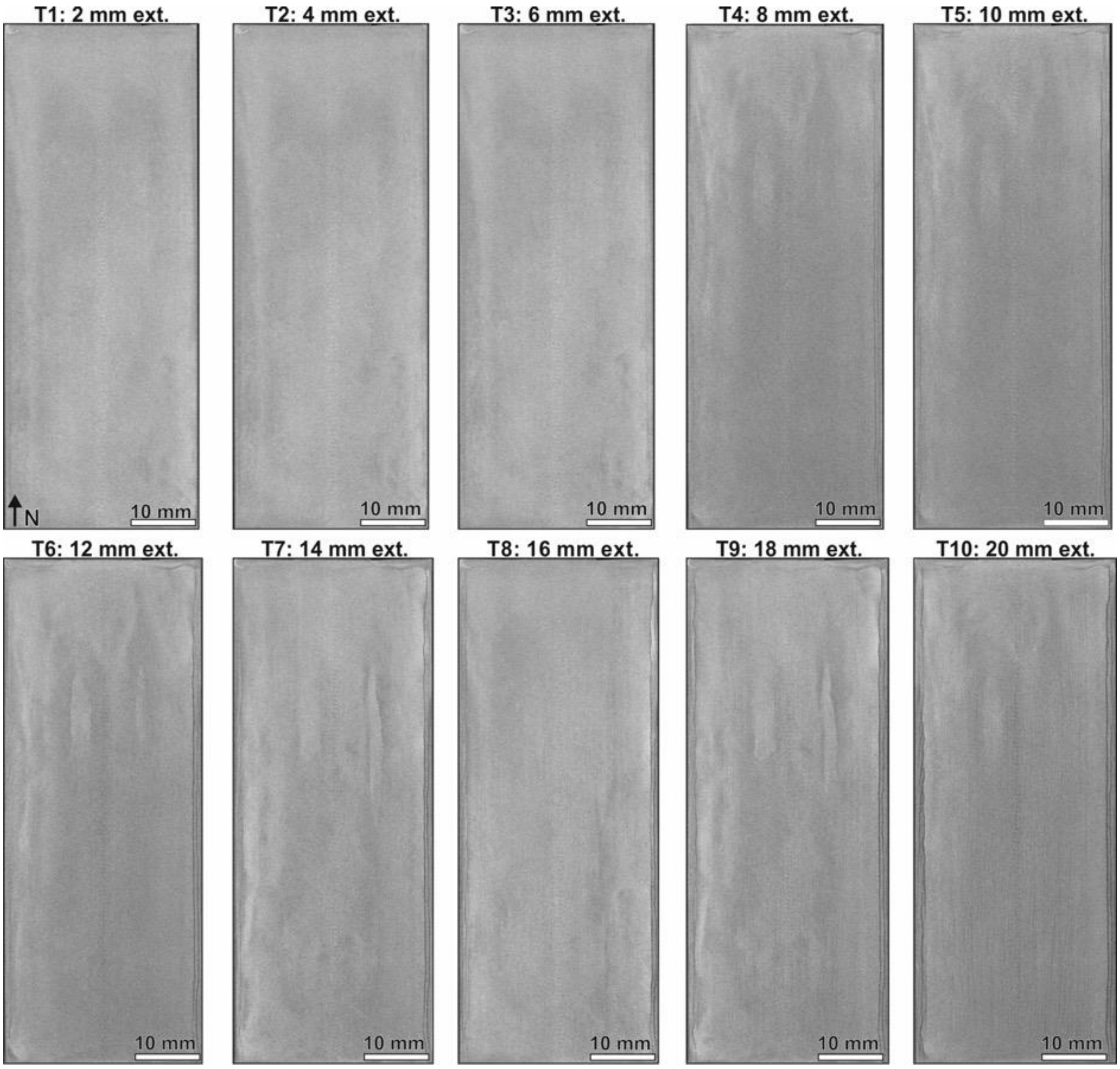

708

709 ***Supplementary figure 8.*** *Top-view results from surface DIC analysis of at every 2 mm of extension from 2*
710 *to 20 mm of extension. Images are showing the upper part of the model (~0.5 cm from the model surface).*
711 *North direction is labelled in T1 and is the same throughout.*

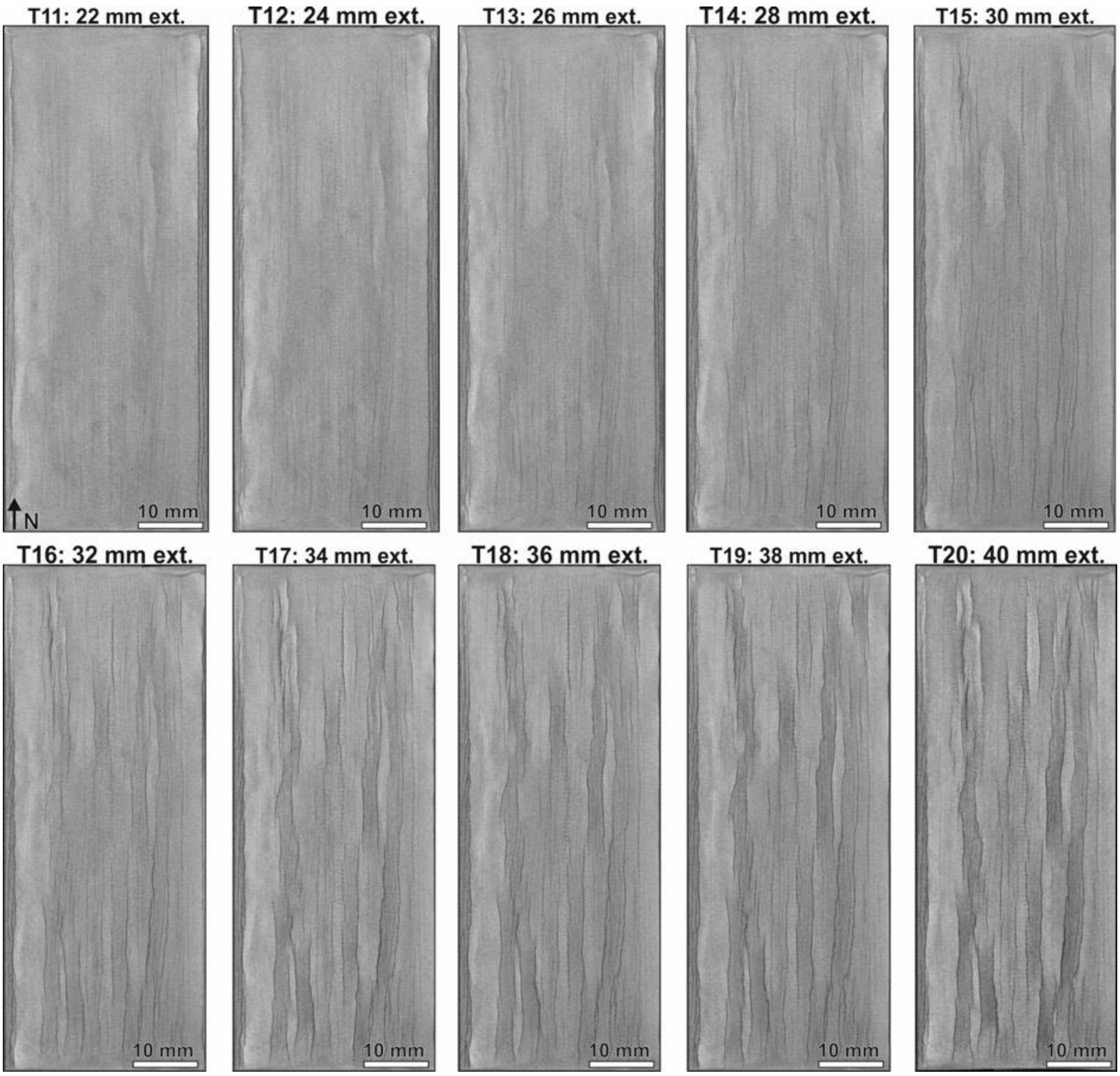

Supplementary figure 9. Top-view results from surface DIC analysis of at every 2 mm of extension from 22 to 40 mm of extension. Images are showing the upper part of the model (~0.5 cm from the model surface). North direction is labelled in T11 and is the same throughout.

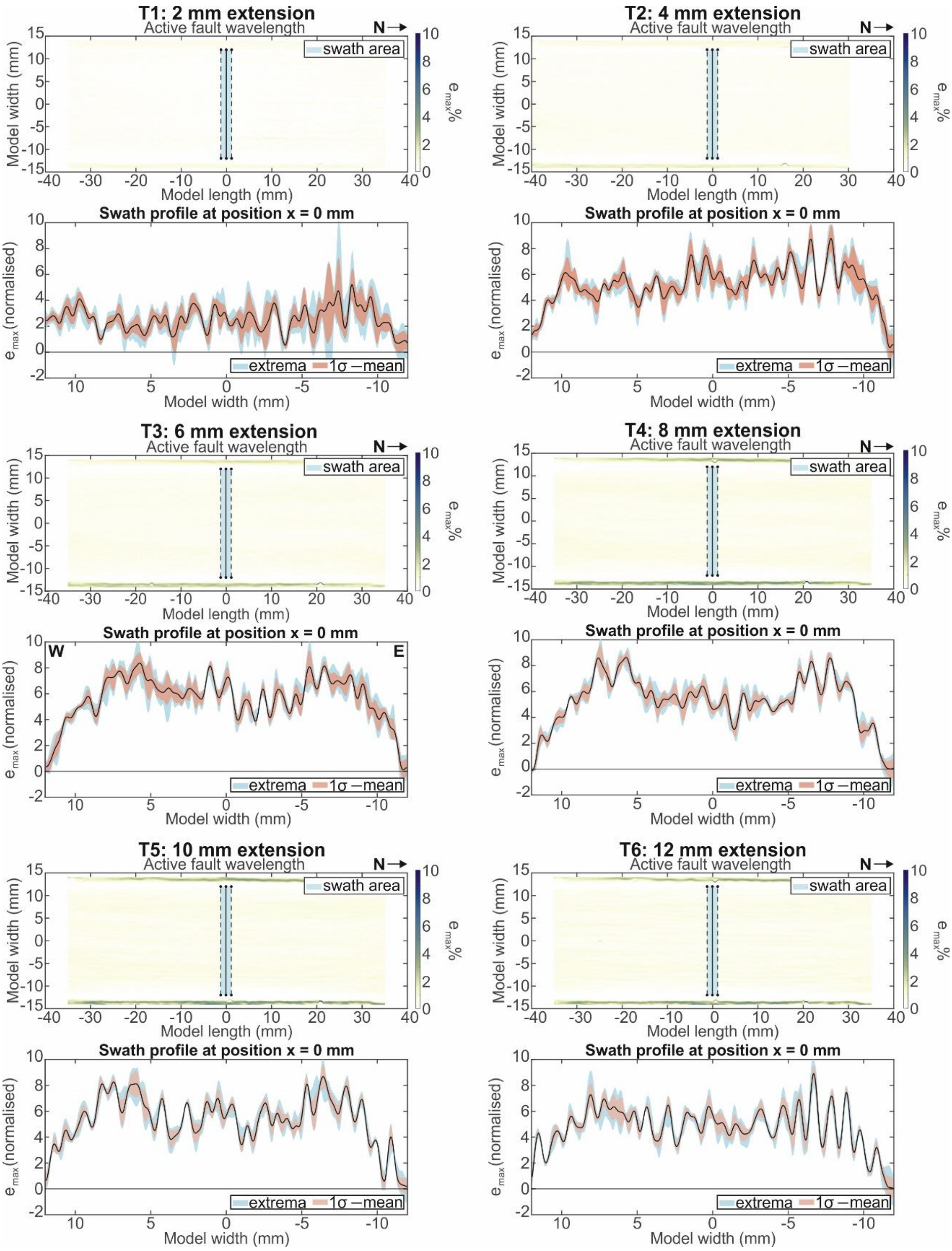

__Supplementary figure 10.__ Swath profiles showing e_{max} (incremental maximum normal strain) to indicate active fault wavelength. e_{max} is normalised using the maximum occurring e_{max} value for better comparison. Profiles are shown every 2 mm of extension from 2-12 mm extension. Each local maximum indicates an active fault. The position of the swath profile is at x=0 mm and has a width of 2 mm. Solid black lines indicate the swath profile mean value. Dark and light blue areas indicate the 1 standard deviation and extrema, respectively.

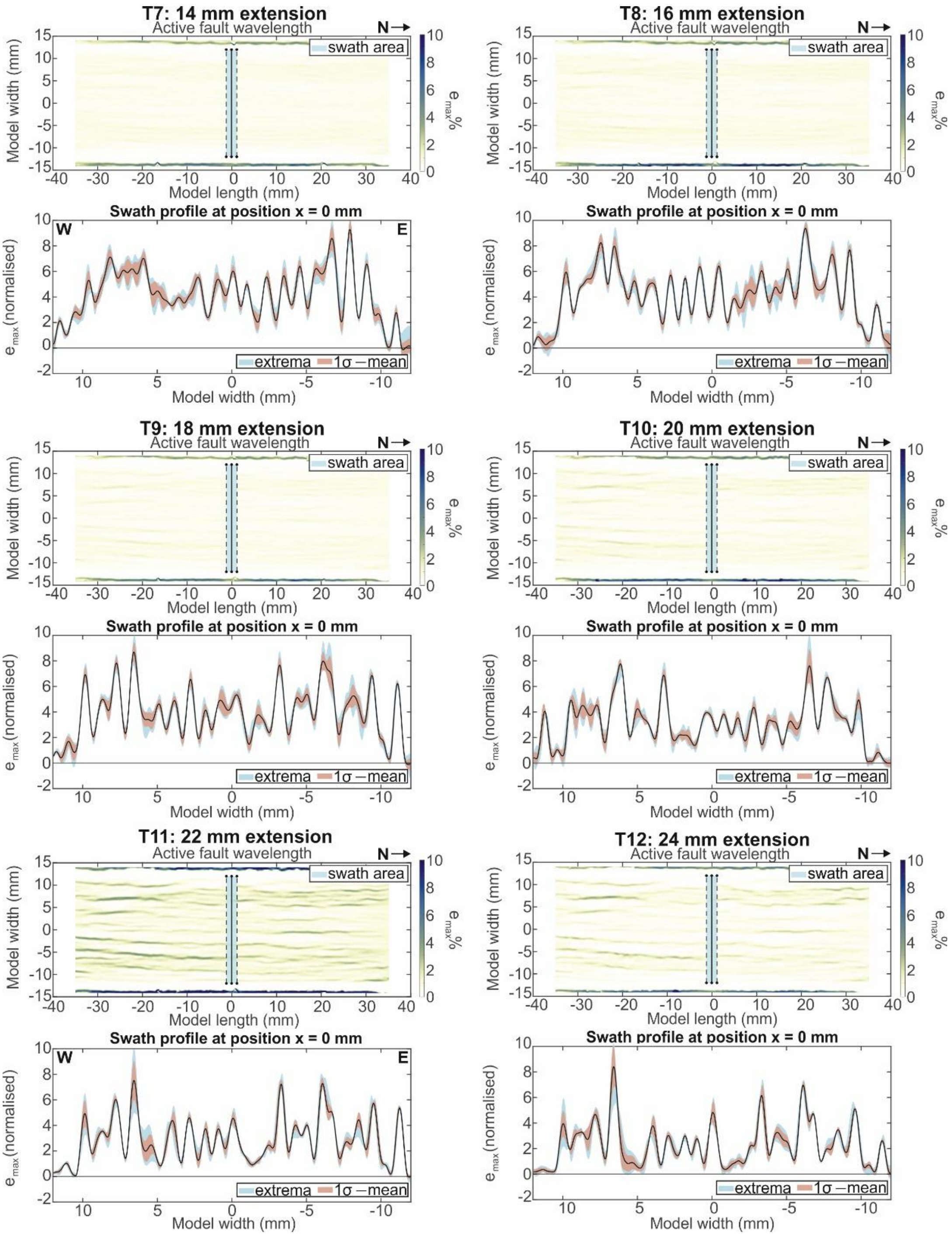

Supplementary figure 11. *Swath profiles showing e_{max} (incremental maximum normal strain) to indicate active fault wavelength. e_{max} is normalised using the maximum occurring e_{max} value for better comparison. Profiles are shown every 2 mm of extension from 14-24 mm extension. Each local maximum indicates an active fault. The position of the swath profile is at x=0 mm and has a width of 2 mm. Solid black lines indicate the swath profile mean value. Dark and light blue areas indicate the 1 standard deviation and extrema, respectively.*

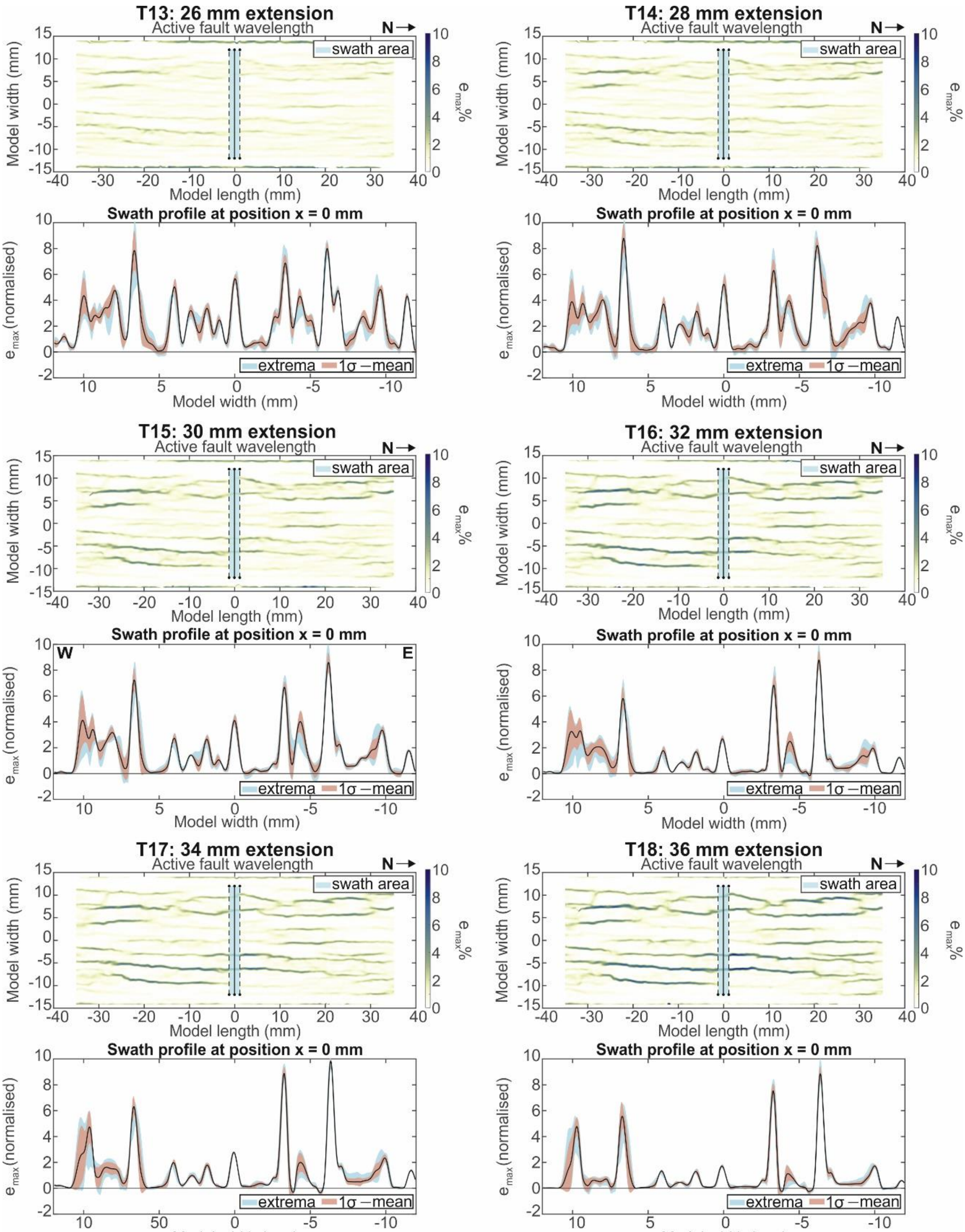

Supplementary figure 12. *Swath profiles showing e_{max} (incremental maximum normal strain) to indicate active fault wavelength. e_{max} is normalised using the maximum occurring e_{max} value for better comparison. Profiles are shown every 2 mm of extension from 16-26 mm extension. Each local maximum indicates an active fault. The position of the swath profile is at x=0 mm and has a width of 2 mm. Solid black lines indicate the swath profile mean value. Dark and light blue areas indicate the 1 standard deviation and extrema, respectively.*

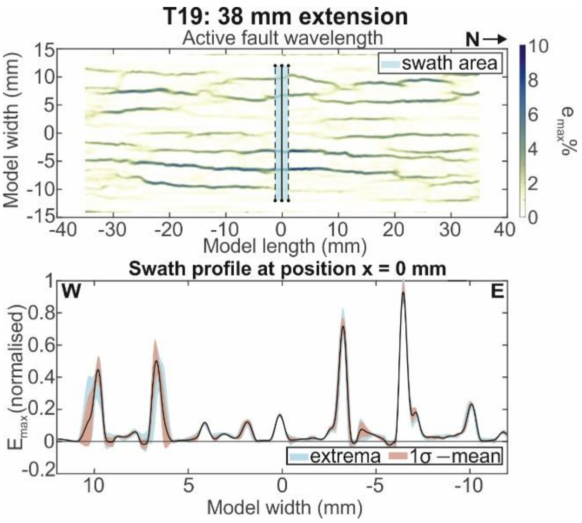

Supplementary figure 13. *Swath profile showing e_{max} (incremental maximum normal strain) to indicate active fault wavelength. e_{max} is normalised using the maximum occurring e_{max} value for better comparison. Profiles is of 38 mm extension. Each local maximum indicates an active fault. The position of the swath profile is at x=0 mm and has a width of 2 mm. Solid black lines indicate the swath profile mean value. Dark and light blue areas indicate the 1 standard deviation and extrema, respectively.*

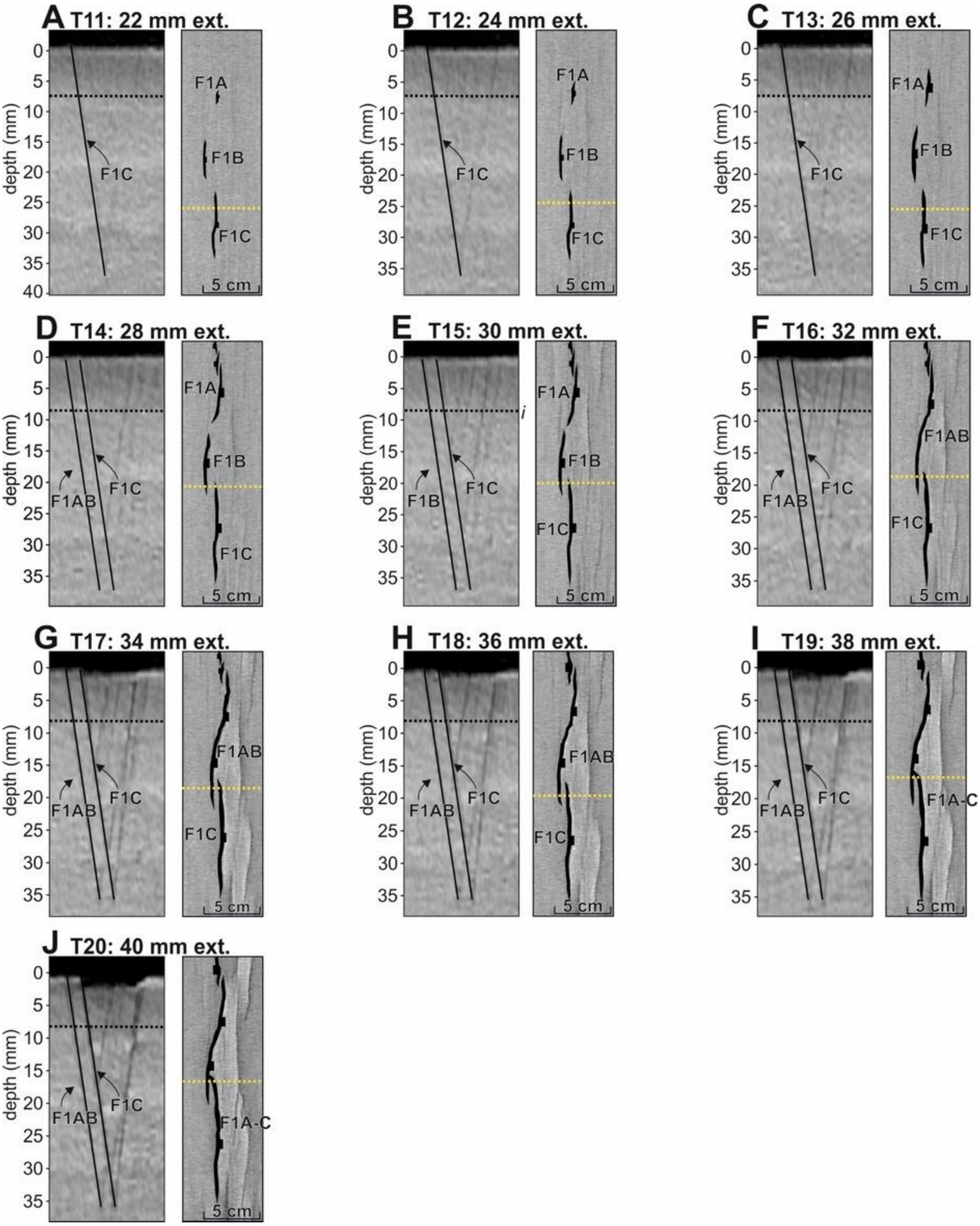

Supplementary figure 14. *Figure showing the growth and segment linkage for Fault 1 from 22 mm extension to 40 mm extension. Faults are shown in cross-section and overhead view. The locations of the cross-sections are indicated by the yellow dashed line on the overhead image. Measurements of fault length are taken at these depths. The location of Fault 1 is labelled in figure 7. Cross-sections have a vertical exaggeration of 1:3.*

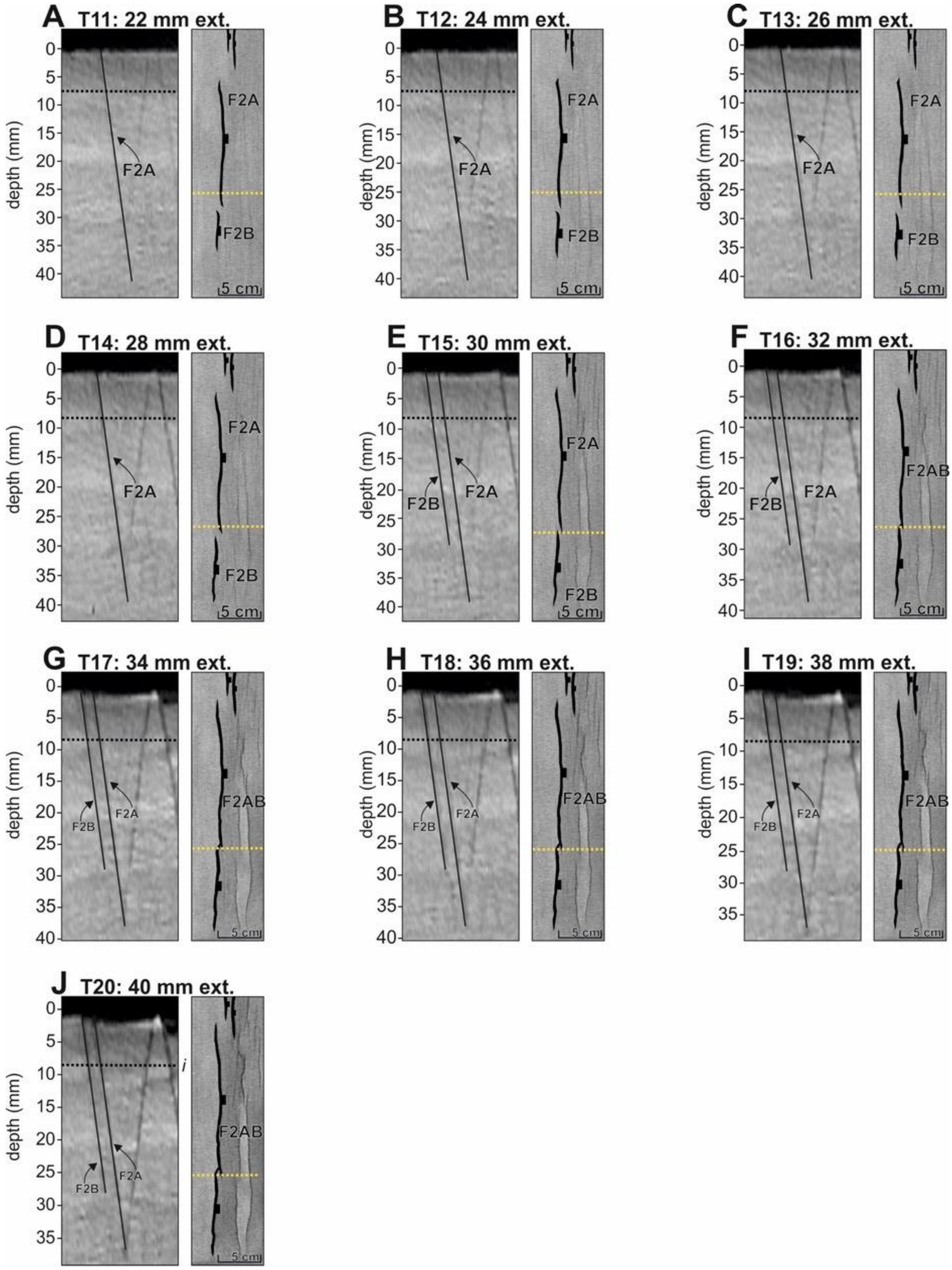

Supplementary figure 15. *Figure showing the growth and segment linkage for Fault 2 from 22 mm extension to 40 mm extension. Faults are shown in cross-section and overhead view. The locations of the cross-sections are indicated by the yellow dashed line on the overhead image. Measurements of fault length are taken at these depths. The location of Fault 2 is labelled in figure 7. Cross-sections have a vertical exaggeration of 1:3.*

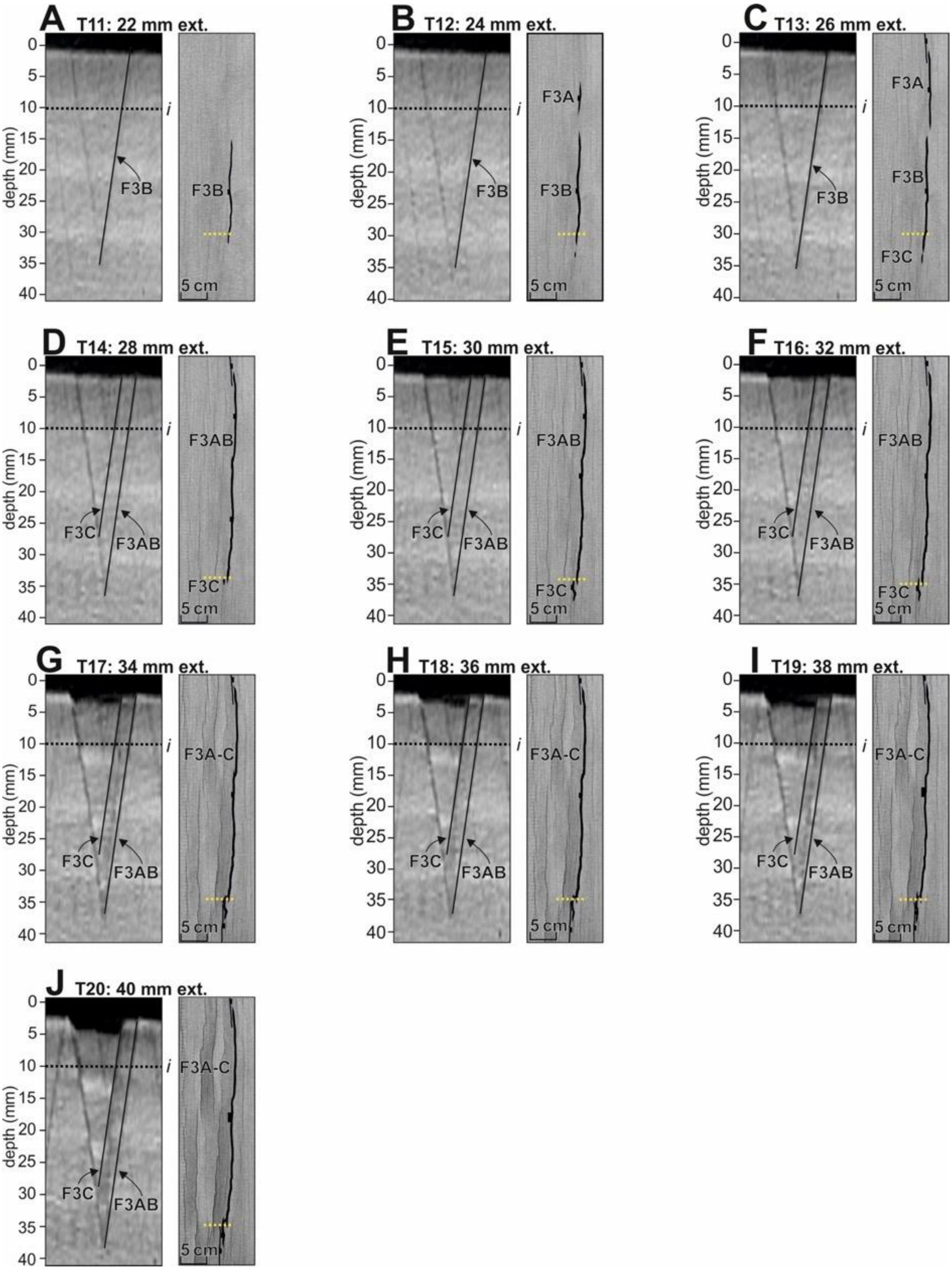

Supplementary figure 16. *Figure showing the growth and segment linkage for Fault 3 from 22 mm extension to 40 mm extension. Faults are shown in cross-section and overhead view. The locations of the cross-sections are indicated by the yellow dashed line on the overhead image. Measurements of fault length are taken at these depths. The location of Fault 3 is labelled in figure 7 of the main text. Cross-sections have a vertical exaggeration of 1:3.*

Exp.	Type	Base	Dimensions	Silicone thickness	Sand thickness	Sidewalls	Extension rate	Extension interval
A	brittle-viscous	5 cm glass 4 cm foam	30 cm x 80 cm	4 cm	4 cm	Yes	400 mm/hr	paused every 2 mm ext.
B	brittle-viscous	5 cm glass 4 cm foam	30 cm x 80 cm	4 cm	6 cm	Yes	800 mm/hr	paused every 2 mm ext.
C	brittle only	8 cm foam	30 cm x 120 cm	n/a	4 cm	No	8 mm/hr	run straight through
D	brittle only	8 cm foam	30 cm x 120 cm	n/a	6 cm	No	8 mm/hr	run straight through

Supplementary table 1. *Parameters in Models A-D.*

References

Adam, J., Urai, J. L., Wieneke, B., Oncken, O., Pfeiffer, K., Kukowski, N., & Lohrmann, J. (2005). Shear localisation and strain distribution during tectonic faulting — new insights from granular-flow experiments and high-resolution optical image correlation techniques. *Journal of Structural Geology*, *27*, 283–301. https://doi.org/10.1016/j.jsg.2004.08.008

Boutelier, D., Schrank, C., & Regenauer-Lieb, K. (2019). 2-D finite displacements and strain from particle imaging velocimetry (PIV) analysis of tectonic analogue models with TecPIV. *Solid Earth*, *10*(4), 1123–1139. https://doi.org/10.5194/se-10-1123-2019

Brune, S., Williams, S. E., Butterworth, N. P., & Müller, R. M. (2016). Abrupt plate accelerations shape rifted continental margins. Nature, 536, 201– 204. https://doi.org/10.1038/nature18319

Buck, W. R. (1991). Models of continental lithospheric extension. Journal of Geophysical Research, 96, 20161– 20178. https://doi.org/10.1029/91JB01485

Carboni, F., Koyi, H., Bicocchi, A., & Barchi, M. R. (2022). Modelling the 4D kinematics of extensional structures developed above discontinuous inclined ductile basal detachments. *Journal of Structural Geology*, *157*. https://doi.org/10.1016/j.jsg.2022.104570

Carlo AG: Carlo Bernasconi AG, Switzerland, company website, available at: https://www.carloag.ch.

Carpenter, M., Williams, J. N., Fagereng, Å., Wedmore, L. N. J., Biggs, J., Mphepo, F., Mdala, H., Dulanya, Z., & Manda, B. (2022). Comparing intrarift and border fault structure in the Malawi Rift: Implications for normal fault growth. *Journal of Structural Geology*, *165*(May), 104761. https://doi.org/10.1016/j.jsg.2022.104761

Cartwright, J. A., Mansfield, C., & Trudgill, B. (1996). The growth of normal faults by segment linkage. *Geological Society Special Publication*, *99*(99), 163–177. https://doi.org/10.1144/GSL.SP.1996.099.01.13

Cartwright, J. A., Trudgill, B. D., & Mansfield, C. S. (1995). Fault growth by segment linkage: an explanation for scatter in maximum displacement and trace length data from the Canyonlands Grabens of SE Utah. *Journal of Structural Geology*, *17*(9), 1319–1326. https://doi.org/10.1016/0191-8141(95)00033-A

Chauvin, B. P., Lovely, P. J., Stockmeyer, J. M., Plesch, A., Caumon, G., & Shaw, J. H. (2018). Validating novel boundary conditions for three-dimensional mechanics-based restoration: An extensional sandbox model example. *AAPG Bulletin*, *102*(2), 245–266. https://doi.org/10.1306/0504171620817154

Childs, C., Manzocchi, T., Nicol, A., Walsh, J. J., Soden, A. M., Conneally, J. C., & Delogkos, E. (2017). The relationship between normal drag, relay ramp aspect ratio and fault zone structure. *Geological Society Special Publication*, *439*, 355–372. https://doi.org/10.1144/SP439.16

Childs, C., Watterson, J., & Walsh, J. J. (1995). Fault overlap zones within developing normal fault systems. *Journal of the Geological Society*, *152*(3), 535–549. https://doi.org/10.1144/gsjgs.152.3.0535

Corti, G., Bonini, M., Conticelli, S., Innocenti, F., Manetti, P., Sokoutis, D., Istituto, C. N. R., Pira, G. La, & Pira, G. La. (2003). Analogue modelling of continental extension: a review focused on the relations between the patterns of deformation and the presence of magma. *EarthArXiv*, *63*, 169–247. https://doi.org/10.1016/S0012-8252(03)00035-7

Cowie, P. A., Gupta, S., & Dawers, N. H. (2000). Implications of fault array evolution for synrift depocentre development: insights from a numerical fault growth model. *Basin Research*, 241–261. https://doi.org/10.1111/j.1365-2117.2000.00126.x

Cowie, P. A. (1998). A healing-reloading feedback control on the growth rate of seismogenic faults. *Journal of Structural Geology*, *20*(8), 1075–1087. https://doi.org/10.1016/S0191-8141(98)00034-0

Cowie, P. A., & Roberts, G. P. (2001). Constraining slip rates and spacings for active normal faults. *Journal of Structural Geology*, *23*(12), 1901–1915. https://doi.org/10.1016/S0191-8141(01)00036-0

Crider, J. G., & Pollard, D. D. (1998). Fault linkage: Three-dimensional mechanical interaction between echelon normal faults. *Journal of Geophysical Research: Solid Earth*, *103*(10), 24373–24391. https://doi.org/10.1029/98jb01353

Dawers, N. H., Anders, M. H., & Scholz, C. H. (1993). Growth of normal faults: displacement-length scaling. In *Geology* (Vol. 21, Issue 12, pp. 1107–1110). https://doi.org/10.1130/0091-7613(1993)021<1107:GONFDL>2.3.CO;2

Densmore, A. L., Dawers, N. H., Gupta, S., Guidon, R., & Goldin, T. (2004). Footwall topographic development during continental extension. *Journal of Geophysical Research*, *109*, 1–16. https://doi.org/10.1029/2003jf000115

Faleide, T. S., Braathen, A., Lecomte, I., Mulrooney, M. J., Midtkandal, I., Bugge, A. J., & Planke, S. (2021). Tectonophysics Impacts of seismic resolution on fault interpretation : Insights from seismic modelling. *Tectonophysics*, *816*(February), 229008. https://doi.org/10.1016/j.tecto.2021.229008

Filbrandt, J. B., Richard, P. D., & Franssen, R. (2007). Fault growth and coalescence: Insights from numerical modelling and sandbox experiments. *GeoArabia*, *12*(1), 17–32. https://doi.org/10.2113/geoarabia120117

Finch, E., & Gawthorpe, R. (2017). Growth and interaction of normal faults and fault network evolution in rifts: Insights from three-dimensional discrete element modelling. *Geological Society Special Publication*, *439*(1), 219–248. https://doi.org/10.1144/SP439.23

Fossen, H., & Rotevatn, A. (2016). Fault linkage and relay structures in extensional settings-A review. *Earth-Science Reviews*, *154*, 14–28. https://doi.org/10.1016/j.earscirev.2015.11.014

Gawthorpe, R. L., & Hurst, J. M. (1993). Transfer zones in extensional basins: their structural style and influence on drainage development and stratigraphy. *Journal - Geological Society (London)*, *150*(6), 1137–1152. https://doi.org/10.1144/gsjgs.150.6.1137

Gawthorpe, R. L., & Leeder, M. R. (2000). Tectono-sedimentary evolution of active extensional basins. *Basin Research*, *12*(3–4), 195–218. https://doi.org/10.1111/j.1365-2117.2000.00121.x

Ge, Z., Gawthorpe, R. L., Rotevatn, A., & Thomas, M. B. (2017). Impact of normal faulting and pre-rift salt tectonics on the structural style of salt-influenced rifts: the Late

Jurassic Norwegian Central Graben, North Sea. *Basin Research*, *29*(5), 674–698. https://doi.org/10.1111/bre.12219

Gupta, A., & Scholz, C. H. (2000). A model of normal fault interaction based on observations and theory. *Journal of Structural Geology*, *22*(7), 865–879. https://doi.org/10.1016/S0191-8141(00)00011-0

Gupta, A., & Scholz, C. H. (1998). Utility of elastic models in predicting fault displacement fields. *Journal of Geophysical Research: Solid Earth*, *103*(B1), 823–834. https://doi.org/10.1029/97jb03009

Handin, J. (1969). On the Coulomb-Mohr failure criterion. Journal of Geophysical Research, 74, 5343– 5348. https://doi.org/10.1029/JB074i022p05343

Hemelsdaël, R., & Ford, M. (2016). Relay zone evolution: A history of repeated fault propagation and linkage, central Corinth rift, *Greece. Basin Research, 28*(1), 34–56. https://doi.org/10.1111/bre.12101

Henstra, G. A., Gawthorpe, R. L., Helland-Hansen, W., Ravnås, R., & Rotevatn, A. (2017). Depositional systems in multiphase rifts: seismic case study from the Lofoten margin, Norway. *Basin Research*, *29*(4), 447–469. https://doi.org/10.1111/bre.12183

Henstra, G. A., Rotevatn, A., Gawthorpe, R. L., & Ravnås, R. (2015). Evolution of a major segmented normal fault during multiphase rifting: The origin of plan-view zigzag geometry. *Journal of Structural Geology*, *74*, 45–63. https://doi.org/10.1016/j.jsg.2015.02.005

Hubbert, M. K. (1937). Theory of scale models as applied to the study of geologic structures. *Geological Society of America Bulletin*, *48*, 1459–1520. https://doi.org/https://doi.org/10.1130/GSAB- 48- 1459

Huggins, P., Watterson, J., Walsh, J. J., & Childs, C. (1995). Relay zone geometry and displacement transfer between normal faults recorded in coal-mine plans. *Journal of Structural Geology*, *17*(12), 1741–1755. https://doi.org/10.1016/0191-8141(95)00071-K

Hus, R., Acocella, V., Funiciello, R., & De Batist, M. (2005). Sandbox models of relay ramp structure and evolution. *Journal of Structural Geology*, *27*(3), 459–473. https://doi.org/10.1016/j.jsg.2004.09.004

Jackson, C. A. L., Bell, R. E., Rotevatn, A., & Tvedt, A. B. M. (2017). Techniques to determine the kinematics of synsedimentary normal faults and implications for fault growth models. *Geological Society Special Publication*, *439*(1), 187–217. https://doi.org/10.1144/SP439.22

Jackson, C. A. L., & Rotevatn, A. (2013). 3D seismic analysis of the structure and evolution of a salt-influenced normal fault zone: A test of competing fault growth models. *Journal of Structural Geology*, *54*, 215–234. https://doi.org/10.1016/j.jsg.2013.06.012

Jaeger, J. C., & Cook, N. G. W. (1976). Fundamentals of rock mechanics. Chapman & Hall, Wiley. https://doi.org/10.1017/S0016 75680 0044897

Kim, Y. S., & Sanderson, D. J. (2005). The relationship between displacement and length of faults: A review. *Earth-Science Reviews*, *68*(3–4), 317–334. https://doi.org/10.1016/j.earscirev.2004.06.003

Lathrop, B. A., Jackson, C. A. L., Bell, R. E., & Rotevatn, A. (2021). Normal Fault Kinematics and the Role of Lateral Tip Retreat: An Example from Offshore NW Australia. *Tectonics*, *40*(5). https://doi.org/10.1029/2020TC006631

Lathrop, B. A., Jackson, C. A., Bell, R. E., Rotevatn, A. (2022). Displacement/Length Scaling Relationships for Normal Faults; a Review, Critique, and Revised Compilation. *Frontiers in Earth Science*, *10*, 1–23. https://doi.org/10.3389/feart.2022.907543

Le Calvez, J. H., & Vendeville, B. C. (2002). Experimental designs to model along- strike fault interaction. *Journal of the Virtual Explorer*. https://doi.org/10.3809/jvirtex.2002.00043

Liang, W., Maestrelli, D., National, I., Corti, G., National, I., & Zou, Y. (2021). Normal fault reactivation during multiphase extension: Analogue models and application to the Turkana depression, East Africa. *Tectonophysics*. https://doi.org/10.1016/j.tecto.2021.228870

Mansfield, C., & Cartwright, J. (2001). Fault growth by linkage: Observations and implications from analogue models. *Journal of Structural Geology*, *23*(5), 745–763. https://doi.org/10.1016/S0191-8141(00)00134-6

Mayolle, S., Soliva, R., Dominguez, S., & Wibberley, C. (2023). Normal fault damage zone growth in map view from analogue models. *Journal of Structural Geology*. https://doi.org/10.1016/j.jsg.2023.104975

McLeod, A. E., Underhill, J. R., Davies, S. J., & Dawers, N. H. (2002). The influence of fault array evolution on synrift sedimentation patterns: Controls on deposition in the strathspey-brent-statfjord half graben, northern North Sea. *AAPG Bulletin*, *86*(6), 1061–1093. https://doi.org/10.1306/61eedc24-173e-11d7-8645000102c1865d

Meyer, V., Nicol, A., Childs, C., Walsh, J. J., & Watterson, J. (2002). Progressive localisation of strain during the evolution of a normal fault population. *Journal of Structural Geology*, *24*(8), 1215–1231. https://doi.org/10.1016/S0191-8141(01)00104-3

Moriya, S., Childs, C., Manzocchi, T., & Walsh, J. J. (2005). Analysis of the relationships between strain, polarity and population slope for Analysis of the relationships between strain, polarity and population slope for normal fault systems. *Journal of Structural Geology*. https://doi.org/10.1016/j.jsg.2005.01.017

Morley, C. K., Nelson, R. A., Patton, T. L., & Munn, S. G. (1990). Transfer zones in the East African rift system and their relevance to hydrocarbon exploration in rifts. *American Association of Petroleum Geologists Bulletin*, *74*(8), 1234–1253. https://doi.org/10.1306/0c9b2475-1710-11d7-8645000102c1865d

Mulugeta, G. (1988). Squeeze box in a centrifuge. Tectonophysics, 148, 323– 335. https://doi.org/10.1016/0040-1951(88)90139-4

Nicol, A., Mouslopoulou, V., Begg, J., & Oncken, O. (2020a). Displacement Accumulation and Sampling of Paleoearthquakes on Active Normal Faults of Crete in the Eastern Mediterranean. *Geochemistry, Geophysics, Geosystems*, *21*(11), 1–22. https://doi.org/10.1029/2020GC009265

Nicol, A., Walsh, J., Berryman, K., & Nodder, S. (2005). Growth of a normal fault by the accumulation of slip over millions of years. *Journal of Structural Geology*, *27*(2), 327–342. https://doi.org/10.1016/j.jsg.2004.09.002

Nicol, A., Walsh, J., Childs, C., & Manzocchi, T. (2020b). The growth of faults. In *Understanding Faults: Detecting, Dating, and Modeling*. Elsevier Inc. https://doi.org/10.1016/B978-0-12-815985-9.00006-0

Osagiede, E. E., Rosenau, M., & Rotevatn, A. (2021). Influence of Zones of Pre-Existing Crustal Weakness on Strain Localization and Partitioning During Rifting: Insights From Analog Modeling Using High-Resolution 3D Digital Image Correlation. *Tectonics*, *40*, 1–30. https://doi.org/10.1029/2021TC006970

Pan, S., Bell, R. E., Jackson, C. A. L., & Naliboff, J. (2021). Evolution of normal fault displacement and length as continental lithosphere stretches. *Basin Research*, *August*. https://doi.org/10.1111/bre.12613

Pan, S., Naliboff, J., Bell, R., & Jackson, C. (2022). Bridging Spatiotemporal Scales of Normal Fault Growth During Continental Extension Using High-Resolution 3D Numerical Models. *Geochemistry, Geophysics, Geosystems*, *23*(7), 1–16. https://doi.org/10.1029/2021GC010316

Panien, M., Schreurs, G., & Pfiffner, A. (2006). Mechanical behaviour of granular materials used in analogue modelling: insights from grain characterisation, ring-shear tests and analogue experiments. *Journal of Structural Geology*, *28*(9), 1710–1724. https://doi.org/10.1016/j.jsg.2006.05.004

Peacock, D. C. P., Nixon, C. W., Rotevatn, A., Sanderson, D. J., & Zuluaga, L. F. (2016). Glossary of fault and other fracture networks. *Journal of Structural Geology*, *92*, 12–29. https://doi.org/10.1016/j.jsg.2016.09.008

Peacock, D. C. P., & Sanderson, D. J. (1994). Geometry and development of relay ramps in normal fault systems. *American Association of Petroleum Geologists Bulletin*, *78*(2), 147–165. https://doi.org/10.1306/bdff9046-1718-11d7-8645000102c1865d

Pickering, G., Peacock, D. C. P., Sanderson, D. J., & Bull, J. M. (1997). Modeling tip zones to predict the throw and length characteristics of faults. *AAPG Bulletin*, *81*(1), 82–99. https://doi.org/10.1306/522b4299-1727-11d7-8645000102c1865d

Ramberg, H. (1981). Gravity, deformation and the earth's crust. Academic Press.

Rotevatn, A., Jackson, C. A. L., Tvedt, A. B. M., Bell, R. E., & Blækkan, I. (2019). How do normal faults grow? *Journal of Structural Geology*, *125*(August 2018), 174–184. https://doi.org/10.1016/j.jsg.2018.08.005

Sahoo, T. R., Nicol, A., Browne, G. H., & Strogen, D. P. (2020). Evolution of a Normal Fault System Along Eastern Gondwana, New Zealand. *Tectonics*, 1–19. https://doi.org/10.1029/2020TC006181

Schlagenhauf, A., Manighetti, I., Malavieille, J., & Dominguez, S. (2008). Incremental growth of normal faults: Insights from a laser-equipped analog experiment. *Earth and Planetary Science Letters*, *273*(3–4), 299–311. https://doi.org/10.1016/j.epsl.2008.06.042

Schmid, T. C., Schreurs, G., & Adam, J. (2022a). Characteristics of continental rifting in rotational systems: New findings from spatiotemporal high resolution quantified crustal scale analogue models. *Tectonophysics*, *822*, 229174. https://doi.org/10.1016/j.tecto.2021.229174

Schmid, T. C., Schreurs, G., & Adam, J. (2022b). Rotational Extension Promotes Coeval Upper Crustal Brittle Faulting and Deep - Seated Rift - Axis Parallel Flow: Dynamic Coupling Processes Inferred Rotational Extension Promotes Coeval Upper Crustal Brittle Faulting and Deep-Seated Rift-Axis Parallel Fl. *Journal of Geophysical Research*, *August*. https://doi.org/10.1029/2022JB024434

Schmid, T., Schreurs, G., Warsitzka, M., Rosenau, M. (2020c): Effect of sieving height on density and friction of brittle analogue material: ring-shear test data of quarz sand used for analogue experiments in the Tectonic Modelling Lab of the University of Bern https://doi.org/10.5880/fidgeo.2020.006

Soliva, R., Benedicto, A., Schultz, R. A., Maerten, L., & Micarelli, L. (2008). Displacement and interaction of normal fault segments branched at depth: Implications for fault growth and potential earthquake rupture size. *Journal of Structural Geology*, *30*(10), 1288–1299. https://doi.org/10.1016/j.jsg.2008.07.005

Soliva, R., & Benedicto, A. (2004). A linkage criterion for segmented normal faults. *Journal of Structural Geology*, *26*(12), 2251–2267. https://doi.org/10.1016/j.jsg.2004.06.008

Trudgill, B., & Cartwright, J. (1994). Relay-ramp forms and normal-fault linkages, Canyonlands National Park, Utah. *Geological Society of America Bulletin*, *106*(September), 1143–1157. https://doi.org/10.1130/0016-7606(1994)106<1143:RRFANF>2.3.CO;2

Tvedt, A. B. M., Rotevatn, A., & Jackson, C. A. L. (2016). Supra-salt normal fault growth during the rise and fall of a diapir: Perspectives from 3D seismic reflection data, Norwegian North Sea. *Journal of Structural Geology*, *91*, 1–26. https://doi.org/10.1016/j.jsg.2016.08.001

Twiss, R. J., & Moore, E. M. (1992). Structural geology. W.H. Freeman and Company. https://doi.org/10.1002/gj.3350290408

Vendeville, B., Cobbold, P. R., Davy, P., Brun, J. P., & Choukroune, P. (1987). Physical models of extensional tectonics at various scales. *Continental Extensional Tectonics*, *28*, 95–107.

Walsh, J. J., Bailey, W. R., Childs, C., Nicol, A., & Bonson, C. G. (2003). Formation of segmented normal faults: A 3-D perspective. *Journal of Structural Geology*, *25*(8), 1251–1262. https://doi.org/10.1016/S0191-8141(02)00161-X

Walsh, J. J., Nicol, A., & Childs, C. (2002). An alternative model for the growth of faults. *Journal of Structural Geology*, *24*(11), 1669–1675. https://doi.org/10.1016/S0191-8141(01)00165-1

Walsh, J. J., & Watterson, J. (1988). Analysis of the relationship between displacements and dimensions of faults. *Journal of Structural Geology*, *10*(3), 239–247. https://doi.org/10.1016/0191-8141(88)90057-0

Wang, L., Maestrelli, D., Corti, G., Zou, Y., & Shen, C. (2021). Normal fault reactivation during multiphase extension: Analogue models and application to the Turkana depression, East Africa. *Tectonophysics*, *811*(March), 228870. https://doi.org/10.1016/j.tecto.2021.228870

Weijermars, R., & Schmeling, H. (1986). Scaling of Newtonian and non- Newtonian fluid dynamics without inertia for quantitative modelling of rock flow due to gravity (including the concept of rheological similarity). Physics of the Earth and Planetary Interiors, 43, 316– 330. https://doi.org/10.1016/0031-9201(86)90021–X

Westerweel, J., & Scarano, F. (2005). Universal outlier detection for PIV data. *Experiments in Fluids*, *39*, 1096–1100. https://doi.org/10.1007/s00348-005-0016-6

Whipp, P. S., Jackson, C. A. L., Schlische, R. W., Withjack, M. O., & Gawthorpe, R. L. (2016). Spatial distribution and evolution of fault-segment boundary types in rift systems: Observations from experimental clay models. *Geological Society Special Publication*, *439*(1), 79–107. https://doi.org/10.1144/SP439.7

Ze, T., & Alves, T. M. (2019). Impacts of data sampling on the interpretation of normal fault propagation and segment linkage. *Tectonophysics*, *762*(March), 79–96. https://doi.org/10.1016/j.tecto.2019.03.013

Zwaan, F., Chenin, P., Erratt, D., Manatschal, G., & Schreurs, G. (2021a). Complex rift patterns, a result of interacting crustal and mantle weaknesses, or multiphase rifting? Insights from analogue models. *Solid Earth*, *12*, 1473–1495. https://doi.org/10.5194/se-12-1473-2021

Zwaan, F., & Schreurs, G. (2021b). Analogue modelling of continental rifting: an overview. *Rifted Margins*, *February*, 0–30. https://doi.org/10.51926/ISTE.5061.6

Zwaan, F., & Schreurs, G. (2017). How oblique extension and structural inheritance influence rift segment interaction: Insights from 4D analog models. *Interpretation*, *5*(1), 119–138. https://doi.org/10.1190/INT-2016-0063.1

Zwaan, F., Schreurs, G., & Buiter, S. J. H. (2019). A systematic comparison of experimental set-ups for modelling extensional tectonics. In *Solid Earth* (Vol. 10, Issue 4). https://doi.org/10.5194/se-10-1063-2019

Zwaan, F., Schreurs, G., Buiter, S. J. H., Ferrer, O., Reitano, R., Rudolf, M., & Willingshofer, E. (2022). Analogue modelling of basin inversion: a review and future perspectives. *Solid Earth*, *13*(12), 1859–1905. https://doi.org/10.5194/se-13-1859-2022

Zwaan, F., Schreurs, G., Naliboff, J., & Buiter, S. J. H. (2016). Insights into the effects of oblique extension on continental rift interaction from 3D analogue and numerical models. *Tectonophysics*, *693*, 239–260. https://doi.org/10.1016/j.tecto.2016.02.036

Zwaan, F., Schreurs, G., & Rosenau, M. (2020). Rift propagation in rotational versus orthogonal extension: insights from 4D analogue models. *Journal of Structural Geology*, *135*. https://doi.org/10.1016/j.jsg.2019.103946

Zwaan, F., Schreurs, G., Ritter, M., Santimano, T., Rosenau, M. (2018). Rheology of PDMS- corundum sand mixtures from the Tectonic Modelling Lab of the University of Bern (CH). GFZ Data Services. https://doi.org/10.5880/fidgeo.2018.023.